UC Santa Barbara
UC Santa Barbara Electronic Theses and Dissertations

Title

Mitigating surface losses and strain in InGaN microLEDs

Permalink

https://escholarship.org/uc/item/9j35m0gk

Author

Ley, Ryan T

Publication Date

2021

Peer reviewed|Thesis/dissertation

University of California
Santa Barbara

Mitigating surface losses and strain in InGaN microLEDs

A dissertation submitted in partial satisfaction
of the requirements for the degree

Doctor of Philosophy
in
Chemical Engineering

by

Ryan T. Ley

Committee in charge:

       Professor Michael Gordon, Chair
       Professor Eric McFarland
       Professor Phillip Christopher
       Professor Steven DenBaars, co-Chair

June 2021

The Dissertation of Ryan T. Ley is approved.

_____

Professor Eric McFarland

_____

Professor Phillip Christopher

_____

Professor Steven DenBaars, co-Chair

_____

Professor Michael Gordon, Committee Chair

May 2021

Curriculum Vitæ
Ryan T. Ley

Education

2021	Ph.D. in Chemical Engineering, University of California, Santa Barbara.
2016	B.S. in Chemical Engineering, Miami University of Ohio

First-Author Publications at UCSB

2020	**R.T. Ley**, J.M. Smith, M.S. Wong, T. Margalith, S. Nakamura, S.P. DenBaars, M.J. Gordon, "Revealing the importance of light extraction efficiency in InGaN microLEDs via chemical treatments and dielectric passivation", *Appl. Phys. Lett.*, **116** (25), 251104 (2020)
2019	**R.T. Ley**, L. Chan, P. Shapturenka, M.S. Wong, S.P. DenBaars, M.J. Gordon, "Strain relaxation of InGaN/GaN multi-quantum well light emitters via nanopatterning", *Opt. Express*, **27** (21), 30081-30089 (2019)

Co-Author Publications at UCSB

2021	S.S. Pasayat, C. Gupta, M.S. Wong, **R.T. Ley**, M.J. Gordon, S.P. DenBaars, S. Nakamura, S. Keller, U.K. Mishra, "Demonstration of ultra-small ($<$ 10 μm) 632 nm red InGaN micro-LEDs with useful on-wafer external quantum efficiency ($>$ 0.2%) for mini-displays", *Appl. Phys. Express*, **117** (14), 011004 (2021)
2020	S.S. Pasayat, **R.T. Ley**, C. Gupta, M.S. Wong, C. Lynsky, Y. Wang, M.J. Gordon, S.P. DenBaars, S. Nakamura, S. Keller, U.K. Mishra, "Color-tunable ¡ 10 μm square InGaN micro-LEDs on compliant GaN-on-porous-GaN pseudo-substrates", *Appl. Phys. Lett.*, **117** (6), 061105 (2020)
2020	J.M. Smith, **R.T. Ley**, M.S. Wong, Y.H. Baek, J.H. Kang, C.H. Kim, M.J. Gordon, S. Nakamura, J.S. Speck, S.P. DenBaars, "Comparison of size-dependent characteristics of blue and green InGaN microLEDs down to 1 μm in diameter", *Appl. Phys. Lett.*, **116** (7), 071102 (2020)
2018	M.S. Wong, D. Hwang, A.I. Alhassan, C. Lee, **R.T. Ley**, S. Nakamura, S.P. DenBaars, "High efficiency III-nitride micro-light-emitting diodes by sidewall passivation using atomic layer deposition", *Opt. Express*, **26** (16), (2018)

Non-UCSB Publications

2017   J.R. Phifer, C.E. Cox, L.F. da Silva, G.G. Nogueira, A.K. Barbosa, **R.T. Ley**, S.M. Bozada, E.J. O'Loughlin, A.S. Paluch, "Predicting the equilibrium solubility of solid polycyclic aromatic hydrocarbons and dibenzothiophene using a combination of MOSCED plus molecular simulation or electronic structure calculations", *Molecular Physics*, **116** (2017)

2017   C.E. Cox, J.R. Phifer, L.F. da Silva, G.C. Nogueira, **R.T.Ley**, E.J. O'Loughlin, A.K. Barbosa, B.T. Rygelski, A.S. Paluch, "Combining MOSCED with molecular simulation free energy calculations or electronic structure calculations to develop an efficient tool for solvent formulation and selection", *J. Comput. Aided Mol. Des.*, **31** 2 (2017)

2017   M.R. Caudle, C.E. Cox, **R.T. Ley**, A.S. Paluch "A molecular study of wastewater contaminants atenolol and atrazine in 1-n-butyl-3-methylimidazolium based ionic liquids for potential treatment applications", *Molecular Physics*, **155** (2017)

2016   **R.T. Ley**, G.B. Fuerst, B.N. Redeker, A.S. Paluch "Developing a predictive form of MOSCED for nonelectrolyte solids using molecular simulation: application to acetanilide, acetaminophen and phenacetin", *Ind. Eng. Chem. Res.*, **55** (18), 5415-5430 (2016)

2016   **R.T. Ley**, A.S. Paluch "Understanding the large solubility of lidocaine in 1-n-butyl-3-methylimidazolium based ionic liquids using molecular simulation", *J. Chem. Phys.*, **144** 084501 (2016)

2015   G.B. Fuerst, **R.T. Ley**, A.S. Paluch "Calculating the fugacity of pure, low volatile liquids via molecular simulation with application to acetanilide, acetaminophen and phenacetin", *Ind. Eng. Chem.*, **54** (2015)

Abstract

Mitigating surface losses and strain in InGaN microLEDs

by

Ryan T. Ley

III-nitride microLEDs have gained much attention as a replacement for organic-LED (OLED) and liquid crystal (LCD)-based displays due to the former's tunable bandgap, high defect tolerance, long lifetimes and superior efficiency. High pixel density, next-generation displays also demand efficient and low cost red-green-blue (RGB) pixels with lateral dimensions below 5 μm, for which OLED and LCD platforms become intractable. Unfortunately, nitride-based LEDs become inefficient as device dimensions shrink due to nonradiative surface states, such as point defects and dangling bonds, which are largely introduced during plasma-based device patterning. Due to high surface-area-to-volume ratios, these effects become ever more important for microLEDs . In addition to the surface recombination loss problem, there are challenges related to growing high quality, high In-content InGaN for full color RGB displays, most notably for red emitters. The 11% lattice mismatch between InN and GaN leads to reduced crystal quality. Moreover, large piezoelectric fields in the III-nitrides reduce the radiative efficiency and lead to poor emission characteristics. The goals of this Ph.D. project were to (i) eliminate surface-related nonradiative recombination losses and (ii) develop strategies for mitigating strain in InGaN/GaN LEDs for improved efficiency and emission characteristics.

Dielectric passivation and chemical treatments have been used to alleviate surface recombination losses; these approaches, however, have mostly focused on devices with lateral dimensions of 20 μm and larger due to fabrication and optical characterization challenges. A new cleanroom processing scheme and high sensitivity optoelectronic test-

ing system were developed in order to fabricate and test ultrasmall microLEDs in the relevant size ranges. Chemical etching and Al_2O_3 dielectric passivation were used to minimize nonradiative sidewall defects in InGaN/GaN microLEDs (mesa diameter 2-100 μm). Analysis of the position and shape of EQE curves for all devices suggested size-independent carrier recombination rate coefficients, suggesting an enhancement in the light extraction efficiency (LEE). These extraction benefits had not been experimentally observed before due to overwhelming surface recombination losses and/or large device dimensions. Ray tracing simulations determined that reducing the mesa diameter increased internal light propagation directionality, leading to fewer total internal reflection (TIR) losses, thus confirming the experimental trend of higher EQE for small devices–a trend that is atypical. Given that device performance may actually increase with decreasing mesa diameters when surface losses are minimized, new device applications become viable. One application is sub-micron LEDs as a post-growth, top-down method of strain mitigation, which has been theorized to have many benefits, but in practice has always been limited by surface losses.

When mesa dimensions are reduced to the sub-micron scale, the average strain state in InGaN/GaN structures may be relieved. However, the mesa diameter-strain relationship is not well known. To investigate this relationship, strain in InGaN/GaN multiple-quantum well (MQW) light emitters was relaxed through a colloidal lithography and top-down plasma etching platform. The colloidal lithography was performed using Langmuir-Blodgett dip-coating with silica masks (d = 170, 310, 690, 960 nm) and a Cl_2/N_2 inductively coupled plasma etch to produce nanorod structures. The InGaN/GaN MQW nanorods were characterized using x-ray diffraction (XRD) reciprocal space mapping (RSM) to quantify the degree of relaxation. A peak relaxation of 32% was achieved in the smallest diameter feature (120 nm after etching). Power-dependent photoluminescence (PDPL) showed blue-shifted quantum well emission, which suggests

a reduced piezoelectric field.

The cleanroom process previously discussed for microLEDs (mesa diameter = 2-100 μm) was scaled down to smaller dimensions. A combined electron beam lithography and photolithography approach will be employed to fabricate these devices, which is currently under development. In addition to device processing, optical characterization techniques are being conducted to better understand key properties of sub-micron LEDs. For instance, a reduced piezoelectric field due to strain relaxation is expected to alter the carrier dynamics and ultimately the overall device behavior. In order to isolate the carrier dynamics from overall device EQE characteristics, time-resolved and time-integrated photoluminescence (PL) spectroscopy experiments will be conducted. Specifically, the PL experiments will be used to decouple changes to the radiative and nonradiative recombination rates as the mesa dimensions are reduced. The dielectric passivation and chemical treatments previously developed will continue to be used to minimize surface recombination losses, which not only lower the radiative efficiency but also have the potential to dominate the carrier dynamics. By altering both the temperature and laser pump power (i.e. carrier density) in passivated mesa structures, the various recombination pathway rates may be decoupled from one another.

Contents

Chapter 1

Introduction

1.1 The birth of GaN

The III-nitride material system did not see significant technological advancement until the 1990s, when Shuji Nakamura published a number of breakthroughs. The basic growth of III-nitride materials by metal-organic chemical vapor deposition (MOCVD) was particularly difficult due to the lack of bulk GaN substrates for homoepitaxy. Conventional MOCVD reactors flow reactant gas precursors at high velocities towards a sapphire substrate, resulting in a turbulent flow regime and highly nonuniform growth. Nakamura's first major breakthrough was the development of his two-flow MOCVD reactor design which enabled laminar flow regime for uniform growth of GaN films on sapphire.[1, 2]

The next major breakthrough was the realization of conductive p-GaN. Akasaki and others had discovered that Mg-doped p-GaN became conductive only after a low energy electron beam irradiation treatment (LEEBI). Nakamura correctly identified hydrogen as the source of Mg passivation in p-GaN and developed a simple high temperature anneal to diffuse out hydrogen impurities.[3, 4]

Finally, Nakamura was able to grow high quality InGaN films on a thick GaN-on-

1

sapphire buffer layer rather than InGaN directly on sapphire.[5] Strong InGaN band-edge emission was observed between 400 nm and 445 nm as opposed to previous InGaN films showing luminescence dominated by deep level defects. Nakamura then put all his developments into a InGaN/GaN double heterostructure p-n junction device and demonstrated the first blue InGaN LED electroluminescence (EL).[6] A few years later, Nakamura also demonstrated the first violet InGaN-based laser diode. InGaN LEDs have continued to show rapid development and commercialization. By combining the blue InGaN LED emission with a yellow cerium-doped yttrium aluminum garnet (Ce:YAG) phosphor, white LED bulb was born and revolutionized the solid-state lighting industry.

1.2   III-nitride materials and devices

Following the development of the blue LED in the 1990s, the III-nitride device applications have exploded owing to their highly attractive material properties. They have a bandgap that is tunable from 0.7 to 6.0 eV; which not only allows visible light In-GaN LEDs and laser diodes (LD) but also AlGaN-based UV light emitters. Moreover, the III-nitrides have also gained much attention for high power transistors due to the wide bandgap and high breakdown field. The polarization properties of AlGaN/GaN heterostructures also allows for the formation of a two-dimensional electron gas (2DEG) to achieve high channel mobility in field effect transistors.

Nowadays, III-nitride LEDs have gained enormous attention for their potential use in display technology. The idea is to shrink down red, green and blue (RGB) LEDs to the microscale so they can form the millions of pixels needed for high resolution displays. Producing efficient RGB InGaN microLEDs is particularly difficult, however, as LEDs lose efficiency as the size is reduced and there are material challenges to growing red emitting material.

1.3   Display technology

State-of-the-art display technology is currently based on thin-film transistor liquid crystal displays (TFT-LCDs) and self-emissive organic LEDs (OLEDs).[7] TFT-LCDs utilize a liquid crystal material sandwiched between two polarizing filters with a backlight source. Without the liquid crystal, the light would be blocked by the two orthogonal polarizers. An electric field is applied to the liquid crystal to change the molecular orientation which rotates the polarization state of light and adjusts the amount of light that passes through the second filter. By rotating the liquid crystal, the relative pixel brightness may be controlled. However, this results in a low overall efficiency as most of the light is filtered out from the final image.

Organic LEDs, on the other hand, are self-emissive materials than emit light directly when current is applied. This allows for a "true black" pixel when the OLEDs are simply turned off. OLEDs also have roll-to-roll printing techniques that enable large scale manufacturing. However, these organic materials have relatively low conductivities that lead to high power consumption and shorter operating lifetimes. These displays also suffer outdoors where they struggle to achieve a high enough brightness to compete with sunlight.

The III-nitrides are well-poised to replace LCDs and OLEDs due to the former's tunable bandgap, high defect tolerance, long lifetimes and superior efficiency. High pixel density, next-generation displays also demand efficient and low cost red-green-blue (RGB) pixels with lateral dimensions below 5 μm, for which OLED and LCD platforms become intractable. Unfortunately, nitride-based LEDs become inefficient as device dimensions shrink due to nonradiative surface states, such as structural imperfections and underco-ordinated atoms, which are largely introduced during plasma-based device patterning. Due to high surface-area-to-volume ratios, these effects become ever more important for
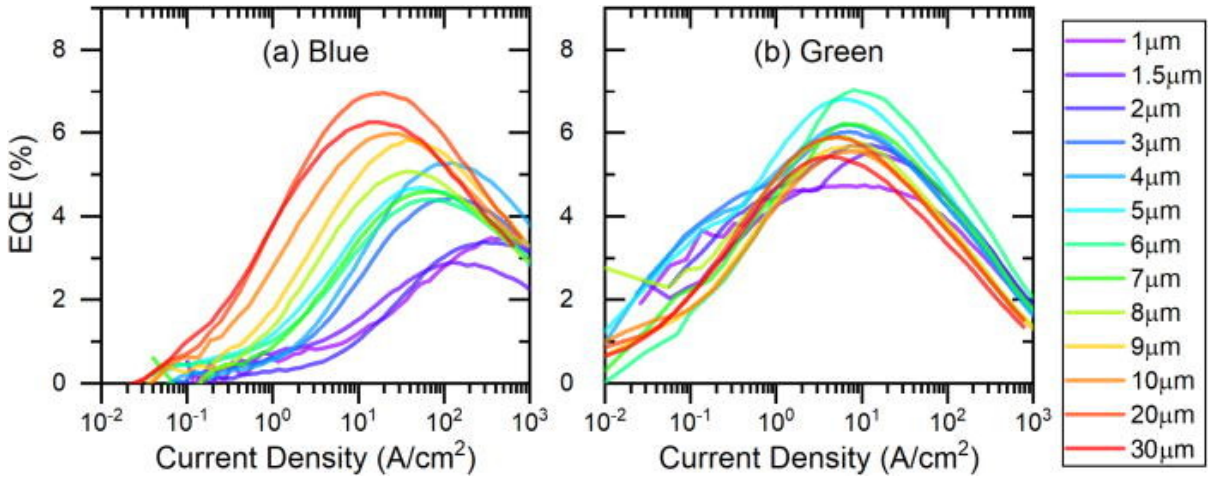
Figure 1.1: EQE curves of microLEDs as a function of mesa diameter for blue and green epi.[8]

microLEDs. In addition to the surface recombination loss problem, there are challenges related to growing high quality, high In-content InGaN for full color RGB displays, most notably for red emitters. The 11 % lattice mismatch InN and GaN leads to reduced crystal quality. Moreover, large piezoelectric fields in the III-nitrides reduce the radiative efficiency and lead to poor emission characteristics.

1.4   Preview of the thesis

In light of the aforementioned issues, my specific project goals are to:

1. Reduce nonradiative surface recombination losses

    (a) Use KOH-based chemical treatments and dielectric passivation to mitigate surface recombination losses

    (b) Design cleanroom processes to fabricate microLEDs with mesa diameters between 1 - 100 μm

    (c) Quantify the optoelectronic properties of ultrasmall microLEDs

4

2. Investigate post-growth, top-down patterning strategies for strain reduction

    (a) Nanopattern InGaN/GaN LED material to engineer the InGaN strain state

    (b) Evaluate the effect of nanopatterning on the strain state and carrier dynamics using x-ray diffraction and photoluminescence techniques

    (c) Extend microLED fabrication processes to sub-micron mesas to quantify the influence of strain relaxation on optoelectronic device properties

Chapter 2 will explore the basic concepts needed to understand the properties InGaN-based microLEDs. The continuity equations that govern semiconductor device behavior are introduced, and surface recombination is constructed from Shockley-Read-Hall theory. Following that, the effect of surface recombination losses on device behavior are then illustrated by solving for the carrier distributions. Finally, passivation methods are discussed with a special focus on KOH-based etching. Chapter 3 will cover the development of microLED cleanroom processing and the implementation of chemical treatments and dielectric passivation to mitigate surface recombination losses. Chapter 4 introduces sub-micron mesa patterning as a route for post-growth strain engineering in InGaN/GaN. X-ray diffraction studies are then used to quantify the strain state as a function of mesa diameter. Chapter 5 combines the concepts of the previous two chapters to fabricate sub-micron LEDs for electrical injection and explore the influence of strain relaxation on carrier dynamics more in depth.

Chapter 2

III-nitride LED physics

2.1 LED device operation

The typical nitride-based LED device structure consists of an active light emitting InGaN layer sandwiched between a Mg doped p-type and Si-doped n-type GaN regions [9] (see Fig. 2.1). Light is generated when electrons in the conduction band recombine with holes in the valence band in the InGaN region, which is referred to as the quantum well layer. Light is generated in an LED when electrons in the conduction band radiatively recombine with holes (or unoccupied electron states) in the valence band. By changing the indium composition of the quantum well, the wavelength of light (or photon energy) may be tuned.

The transport and dynamics of carriers in LED structures is governed by the continuity equations of electrons and holes:

$$\frac{\partial n}{\partial t} = G_n - U_n + \frac{1}{q} \boldsymbol{\nabla} \cdot \boldsymbol{J_n} \tag{2.1}$$

$$\frac{\partial p}{\partial t} = G_p - U_p - \frac{1}{q} \boldsymbol{\nabla} \cdot \boldsymbol{J_p} \tag{2.2}$$
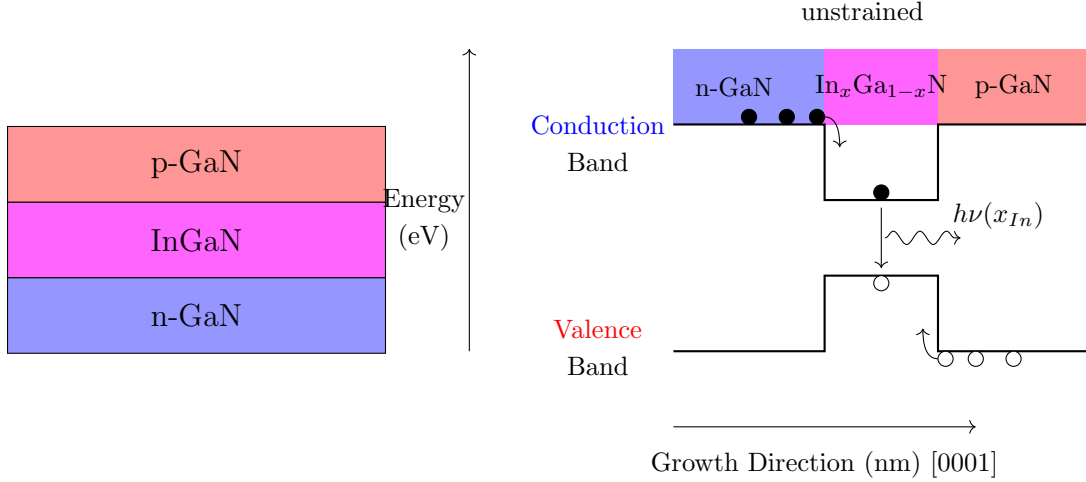
Figure 2.1: (left) Typical LED device structure and (right) a schematic of electron-hole recombination in an energy diagram.

where $\boldsymbol{J_{n,p}}$ is the electron/hole current density, G is the generation rate and $U_{n,p}$ is the recombination rate (both radiative and nonradiative). The electron and hole current density can be described by the drift-diffusion equations:

$$\boldsymbol{J_n} = q\mu_n\boldsymbol{\mathcal{E}} + qD_n\boldsymbol{\nabla}n \tag{2.3}$$

$$\boldsymbol{J_p} = q\mu_p\boldsymbol{\mathcal{E}} - qD_n\boldsymbol{\nabla}p \tag{2.4}$$

where μ is the carrier mobility, D is the diffusion constant, $\boldsymbol{\mathcal{E}}$ is the electric field, n and p are carrier concentrations and q is the fundamental electron charge. The first term is known as the drift current and the second is the diffusion current.

Electrons and holes can recombine with each other either radiatively or nonradiatively. Radiative recombination, where photons are produced, occurs when conduction band electrons spontaneously recombine with empty hole states in the valence band. Nonradiative recombination mechanisms are generally broken down into defect recombination and Auger recombination processes. As the main loss mechanism in microLEDs is bulk and surface defect recombination, those mechanisms will be discussed in detail.

7

2.2   Shockley-Read-Hall nonradiative recombination

Defects in the crystal introduce energy states, E_T, within the semiconductor bandgap. The four possible transitions are (a) electron capture, (b) electron emission, (c) hole capture and (d) hole emission (see Figure 2.2) Each carrier capture and emission process
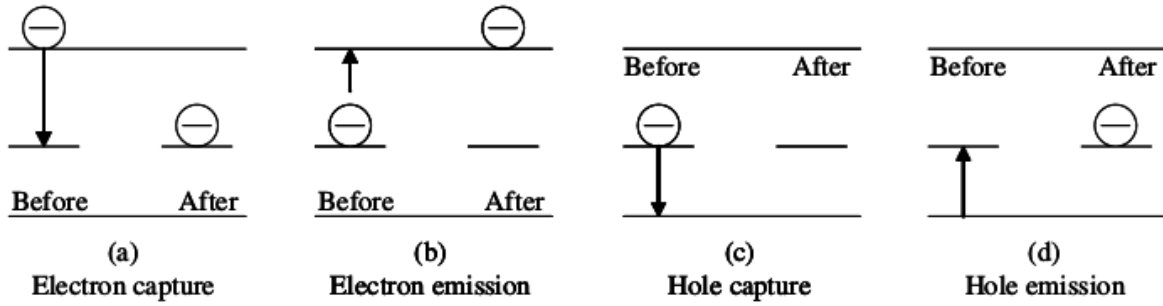

Figure 2.2: Possible electron and hole transitions with a defect at energy level, E_T.

affects the bulk carrier concentration. Transitions (a) and (b) affect the electron concentration, whereas (c) and (d) affect the hole concentration. This allows us to write the time rate of change of the respective carrier concentrations as:

$$\left.\frac{\partial n}{\partial t}\right|_{U-G} = \left.\frac{\partial n}{\partial t}\right|_a + \left.\frac{\partial n}{\partial t}\right|_b \tag{2.5}$$

$$\left.\frac{\partial p}{\partial t}\right|_{U-G} = \left.\frac{\partial p}{\partial t}\right|_c + \left.\frac{\partial p}{\partial t}\right|_d \tag{2.6}$$

Each process can be described by a second order kinetic rate equation where in general $rate \propto$ [carrier A in trap][free carrier B]. Capture events have a rate coefficient $c_{n,p}$ and emission events have a rate coefficient $e_{n,p}$ such that

$$r_N \equiv \left.\frac{\partial n}{\partial t}\right|_{U-G} = c_n p_T n - e_n n_T \tag{2.7}$$

$$r_P \equiv \left.\frac{\partial p}{\partial t}\right|_{U-G} = c_p n_T p - e_p p_T \tag{2.8}$$

8

where p_T and n_T are the concentrations of trapped carriers. Under thermal equilibrium, the net recombination of carriers must be zero ($r_N = r_P = 0$). All the concentrations and coefficients in Eq. (2.8) adopt a subscript "0" to denote thermal equilibrium. Substituting ($r_N = r_P = 0$) into Eq. (2.8) and solving for the emission coefficients provides the expressions

$$e_{n0} = \frac{c_{n0} p_{T0} n_0}{n_{T0}} = c_{n0} n_1 \tag{2.9}$$

$$e_{p0} = \frac{c_{p0} n_{T0} p_0}{p_{T0}} = c_{p0} p_1 \tag{2.10}$$

where n_1 and p_1 are thermal equilibrium concentrations of carriers being excited into the midgap energy state E_T, which are readily computable from Fermi-Dirac statistics.

The next major assumption is that the values of the emission and capture coefficients remain fixed under inherently nonequilibrium device operation conditions. This is hard to assess experimentally, but the available data suggest this is the case except for extreme conditions. Moving forward, rate coefficients will drop the "0" subscript.

Typical device operating conditions are also assumed to be in a quasi-steady state. This approximation is commonly invoked in analyses of semiconductor devices by assuming the fundamental carrier transitions occur on significantly shorter time scales than external changes to the device. This is a reasonable assumption considering that changes to LED operation will likely occur over microsecond to millisecond time scales, whereas carrier transitions occur over nanosecond or shorter time scales. We also define the relationship $p_T = N_T - n_T$, where N_T is the total number of trap states at E_T. Setting $r_N = r_P$ and solving for n_T, we obtain:

$$n_T = \frac{c_n N_T n + c_p N_T p_1}{c_n (n + n_1) + c_p (p + p_1)} \tag{2.11}$$

This expression is then plugged into $r_N = c_n p_T n - e_n n_T$ and, with some algebraic manipulation, we arrive at an expression for the net nonradiative recombination rate $U_{SRH} = r_N = r_P$:

$$U_{SRH} = c_n n \left(N_T - n_T \right) - n_T n_1 c_n \tag{2.12}$$

$$= \frac{np - n_i^2}{\frac{1}{c_p N_T}(n + n_1) + \frac{1}{c_n N_T}(p + p_1)} \tag{2.13}$$

$$= \frac{np - n_i^2}{\tau_p(n + n_1) + \tau_n(p + p_1)} \tag{2.14}$$

where τ is the nonradiative recombination lifetime.

2.3   Surface recombination

The sidewall of an LED mesa is a terminated crystal where the perfect periodic lattice structure is interrupted, which results in structural imperfections and undercoordinated atoms. This gives rise to a continuum of surface defect energy levels throughout the bandgap. We now change the single level defect energy, E_T, to a density of surface defect energy levels, $D_{IT}(E)$.

The parameters used in the previous section are now re-labelled with subscripts "s". Following Eq. (2.14), the surface recombination rate is represented by the following integral:

$$U_s = \int dE \left(\frac{np - n_i^2}{\frac{1}{c_{ps}}(n_s + n_{1s}) + \frac{1}{c_{ns}}(p_s + p_{1s})} \right) D_{IT}(E) \tag{2.15}$$

where p_{1s} and n_{1s} are also functions of energy. $1/c_{ps}$ and $1/c_{ns}$ may be viewed as the surface recombination velocities for electrons and holes, respectively. However, Eq. (2.15) is impractical because the energy dependencies of D_{IT} and the capture coefficients are very difficult to experimentally determine. Instead, an effective surface recombination
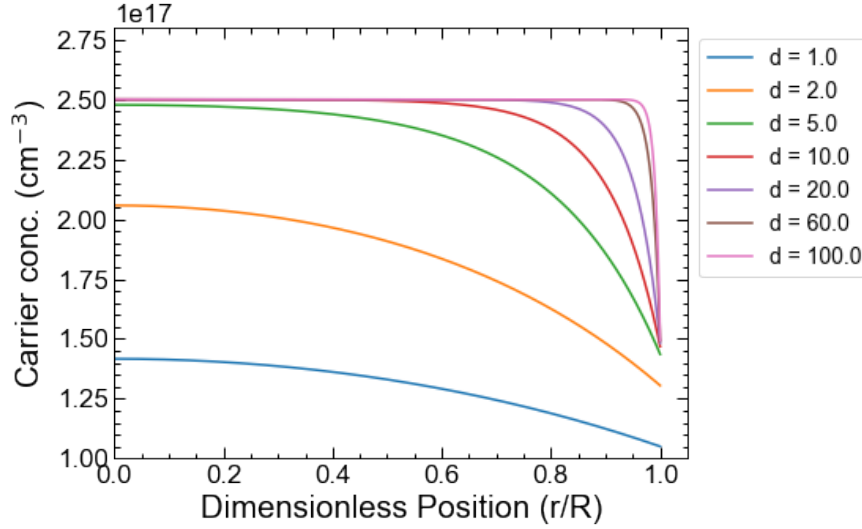
Figure 2.3: Calculated carrier density distributions from Eq. (2.22) for different mesa diameters. S is set to $3.0{\cdot}10^5$ cm/s, τ is $1.0{\cdot}10^{-9}$ s, t_{AR} is 5 nm, D is 2.0 cm^2/s and J is 20 A/cm^2. The dimensionless position, r/R is the position, r, normalized to the total mesa radius, R.

velocity coefficient, S, is determined for both electrons and holes. Time-resolved photoluminescence experiments in GaN (and other semiconductors) have determined this value to be roughly $3.0{\cdot}10^4$ cm/s for pristine GaN surfaces by fitting data the continuity equations with boundary condition:

$$D\frac{\partial n}{\partial r}\bigg|_{r=R} = Sn\bigg|_{r=R} \tag{2.16}$$

where D is the ambipolar diffusion constant for electrons and holes.

To understand the effect of surface recombination losses on microLED behavior, a simplified version of the continuity equations may be solved. The drift-diffusion equations are plugged into the steady-state continuity equations while assuming the electron and hole excess carrier densities are equal ($n = p = N$). The generation rate under electrical injection is $J_{inj}/qt_{AR}D$, where J_{inj} is the injected current density and t_{AR} is the active region thickness. The overall recombination rate may also be simplified to:

11

$$U = \frac{N(r)}{D\tau} \tag{2.17}$$

where τ is the effective carrier lifetime:

$$\frac{1}{\tau} = \frac{1}{\tau_{rad}} + \frac{1}{\tau_{SRH}} + \frac{1}{\tau_{Auger}} \tag{2.18}$$

Putting everything together for a rotationally symmetric cylindrical mesa of radius R, we arrive at the following ordinary differential equation:

$$\frac{d^2N}{dr^2} + \frac{1}{r}\frac{dN}{dr} - \frac{N(r)}{L_n^2} = \frac{J_{inj}}{qt_{AR}D} \tag{2.19}$$

where $L_n^2 = D\tau$ is the carrier diffusion length. We then impose the following boundary conditions:

$$\left.\frac{dN}{dr}\right|_{r=0} = 0 \tag{2.20}$$

$$\left.D\frac{dN}{dr}\right|_{r=R} = -SN(R) \tag{2.21}$$

This equation may be solved analytically to yield:

$$N(r) = \frac{J_{inj}\tau}{qt_{AR}}\left(1 - \frac{\tau S I_0(r/L_n)}{\tau S I_0(R/L_n) + L_n I_1(R/L_n)}\right) \tag{2.22}$$

where I_n is the n-th order modified Bessel function.

2.4   Surface passivation methods

Surface passivation in the context of microLEDs is any attempt to reduce nonradiative surface recombination losses. For this, there are two basic fundamental approaches–

directly reduce the interface state density or limit the excess carrier concentration at the surface. Directly reducing the interface state density, sometimes referred to as chemical passivation, involves minimizing the structural imperfections at the surface, removing any contaminations and depositing a material to improve the bonding configuration of surface atoms. MicroLED mesa sidewalls are rather unpleasant surfaces as they must be formed by a dry etch process due to the inert chemical nature and strong bond energies of the III-nitrides compared to other III/V materials. The dry etch process uses a high energy chlorine-based plasma that combines chemical etching and physical sputtering to remove material. While this process provides control over the etch profile with negligible undercutting of the etch mask, dry etching also damages and contaminates the crystal surface.[] The interface state density, D_{IT} has been shown to increase by an order of magnitude upon exposure the inductively-coupled plasmas (ICP) on AlGaN-insulator transistor gate dielectric surface using photo-assisted capacitance-voltage methods. Solution-based chemical etches are ill-suited for the full mesa formation; however, they have great a potential to be used after the dry etch to clean and remove the outer plasma damaged layer of a mesa.

Wet-chemical etching methods were initially developed for surface roughening in order to improve the light extraction efficiency for solid-state lighting applications. These methods employed a KOH-based photoelectrochemical (PEC) etch in order to produce hexagonal pyramid structures on the N-face of broad area LEDs after substrate removal. These etches are again drawing interest as routes to remove plasma etch damage in microLED devices.

The exact mechanism of how KOH etches away III-nitride material is somewhat controversial. However, it is widely believe to occur through an oxidation and subsequent

dissolution. In one variation, the oxide formation is thought to occur by:

$$2\,\mathrm{GaN} + 3\,\mathrm{H_2O} \longrightarrow \mathrm{Ga_2O_3} + 2\,\mathrm{NH_3} \qquad \{1\}$$
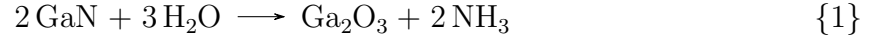
X-ray photoelectron spectroscopy (XPS) studies on Ga-polar and N-polar GaN found $\mathrm{Ga{-}O}$ and $\mathrm{Ga{-}OH}$ bonds after etching in KOH, suggesting that hydroxide ions adsorb to the GaN surface to form gallium oxide with KOH acting as a catalyst. Another proposed etch mechanism proceeds via an electrochemical process where the concentration and transport of carriers plays an important role:

$$2\,\mathrm{GaN} + 6\,\mathrm{h^+} \longrightarrow 2\,\mathrm{Ga^{3+}} + \mathrm{N_2} \qquad \{2\}$$

$$6\,\mathrm{H^+} + 6\,\mathrm{e^-} \longrightarrow 3\,\mathrm{H_2} \qquad \{3\}$$
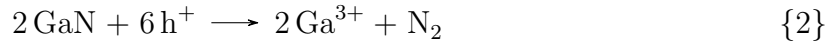
In this case, an excited electron in the conduction band transports to the GaN-KOH interface and then reacts with $\mathrm{H^+}$ to form an oxide. Both proposed mechanisms are possible given the observed trends in the etch behavior as temperature and concentration are changed.

The KOH etch is very anisotropic and highly dependent on the expose crystal plane. As the $\mathrm{OH^-}$ ions must attack the Ga sites for oxidation to occur. Little to no etching occurs on the +c (0001) plane, or Ga-polar plane, because the N atoms block $\mathrm{OH^-}$ from reaching any Ga atoms. On the -c (000$\overline{1}$) plane, or N-polar plane, KOH etching produces hexagonal pyramids. Studies on the facet morphology have shown hexagonal pyramids with side angles of about 58-60°, which suggests that the 10$\overline{1}\overline{1}$ planes are exposed. Changing the temperature and concentration of the KOH etch tends to expose the same crystal planes but rather affects the size and density of the hexagonal facets. If the etch rate is related to the inverse of pyramid density, then the reaction rate follows

an Arrhenius dependence:

$$\frac{1}{\rho} = \frac{1}{\rho_0} e^{-E_a/k_B T} \tag{2.23}$$

where ρ is the pyramid density, E_a is the activation energy, k_B is Boltzmann's constant and T is temperature. A wide range of activation energies have been reported which is likely due to variations in crystal quality and doping across the literature.

2.5   Conclusion

In this chapter, we have discussed how surface recombination losses impact microLED devices. LED device behavior may be described by the continuity equations, where surface recombination becomes a boundary condition. By incorporating the surface recombination boundary condition to the continuity equations, the effect on carrier distributions was illustrated. The goal of many microLED efforts is to minimize the nonradiative losses at sidewall. KOH-based etching has drawn much attention as a route for reducing surface recombination losses. The outer, plasma damaged layer of material is removed, exposing more stable crystallographic facets. These facets may then facilitate the growth of a dielectric-semiconductor interface with a lower defect density.

Chapter 3

Revealing enhanced light extraction in microLEDs

Portions of this chapter have been adapted from [10]

3.1 Introduction

III-nitride microLEDs have gained much attention as a replacement for organic-LED (OLED) and liquid crystal (LCD) based displays due to the former's tunable bandgap,[11] high defect tolerance,[12] long life and superior efficiency.[13] High pixel density, next-generation displays also demand efficient, low cost RGB pixels with lateral dimensions below 5 μm, for which OLED and LCD platforms become intractable.[7, 14] Unfortunately, nitride-based LEDs become inefficient as device dimensions shrink due to nonradiative recombination losses at exposed surfaces.[15–18] These losses originate from nonradiative surface states, such as point defects and Ga dangling bonds,[9, 19] that are largely introduced during plasma-based device patterning[20]. Due to high surface-area-to-volume ratios, these effects become ever more important for microLEDs.
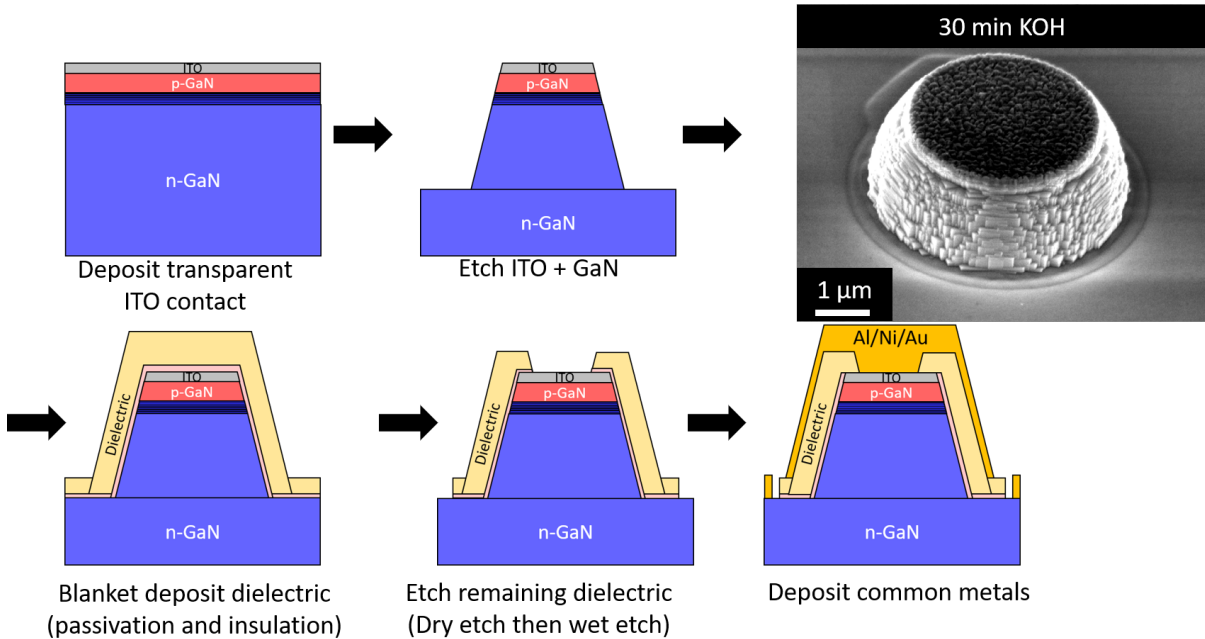
16

Figure 3.1: Simplified device schematic of fully fabricated microLED (a) and an SEM image of a 2 μm mesa structure after room temperature KOH etching (b).

Olivier *et al.* measured the external quantum efficiency (EQE) of electrically injected nitride LEDs using backside emission and found that small devices (10×10 μm^2) had EQEs that were half that of larger devices (500×500 μm^2).[16] Analysis of EQE curves suggested that the Shockley-Read-Hall (SRH) recombination rate rose by over an order of magnitude when device dimensions dropped below 50×50 μm^2. Additional data fitting determined that higher-order Auger recombination losses were approximately the same for LEDs $\leq 100 \times 100$ μm^2.[17] In another work, Smith *et al.* developed a fabrication process that minimized external processing influences on the surface-related peak EQE reduction and reported that EQE losses occur for devices with mesa diameters $< 10\mu$m.[8]

Dielectric passivation and solution-based chemical etching have been quite successful in mitigating the aforementioned problems in microLEDs; these approaches, however, have mostly focused on photoluminescence (PL)[21, 22] or electroluminescence (EL) in devices with lateral dimensions $\geq 10 - 20$ μm due to fabrication and characterization
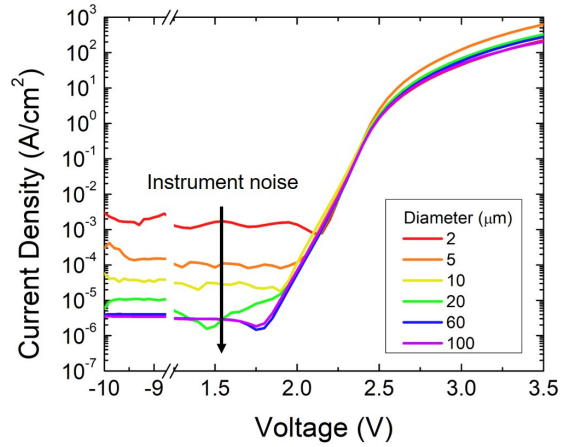
Figure 3.2: Current density-voltage characteristics of a set of microLED device sizes. Current density is based on the area of the active region.

challenges.[23, 24] For example, Wong *et al.* demonstrated that EQE could be increased in LED devices using heated KOH treatments and atomic layer deposition (ALD) of an SiO_2 passivation layer.[23, 24] Most microLED reports have focused on internal efficiency contributions to EQE, despite early observations suggesting increased extraction efficiency.[25] Modeling studies have indeed predicted higher extraction from microLEDs as the mesa size is decreased, but extraction benefits have not been experimentally observed due to overwhelming surface recombination losses and/or large device dimensions.[26]

In the present study, InGaN/GaN microLEDs were fabricated with mesa diameters down to 2 μm to determine if nonradiative recombination losses associated with surface defects could be minimized by incorporating chemical etching and dielectric passivation in LED processing. Devices were measured in a backside emission configuration at current densities down to 0.1 A/cm^2 (where SRH losses dominate) to assess the effect of sidewall defects on EQE.

3.2   Nanofabrication of microLED devices

MicroLED devices (see Fig. 3.1, with mesa diameters of 2-100 μm) were fabricated on commercially grown InGaN/GaN multiple-quantum well (MQW) LED structures (Seoul Viosys) on single-side polished c-plane sapphire. Peak emission wavelengths ranged from 455-470 nm depending on excitation current density. A 60 nm blanket indium-tin-oxide (ITO) transparent p-contact was then deposited by heated electron beam deposition. The mesa etching step consisted of a $CH_4/H_2/Ar$ reactive ion etch (RIE) of ITO, followed by an inductively-coupled Cl_2/N_2 plasma (ICP) etch of the InGaN/GaN layers. The sample was then subjected to a short $SiCl_4$ RIE treatment to minimize contact resistance.[27] A room temperature KOH etch was then conducted for approximately 30 minutes to remove plasma damage as well as expose nanoscale $\{10\bar{1}0\}$ facets on mesa sidewalls. Figure 3.1 shows the scanning electron microscope (SEM) image of the mesa after KOH etching. 20 nm of ALD Al_2O_3 (TMA + H_2O) was then deposited at 300°C to passivate remaining sidewall dangling bonds, followed by plasma-enhanced chemical vapor deposition (PECVD) of Si_3N_4 (250 nm) at 250°C for electrical insulation. Vias were then etched to expose the ITO and n-GaN for metal contacts. The Si_3N_4 was dry etched in a $CHF_3/CF_4/O_2$ ICP and the the Al_2O_3 layer was selectively wet etched for 30 minutes with AZ300MIF photoresist developer. Finally, Al/Ni/Au (500/100/500 nm) metal contacts were deposited by electron beam deposition such that mesa structures were completely covered with metal. DC current-voltage (I-V) characteristics were measured using a Keithley 2400 source meter. I-V tests were conducted in forward bias from 0 to 3.5 V and in reverse bias from 0 to -10 V.
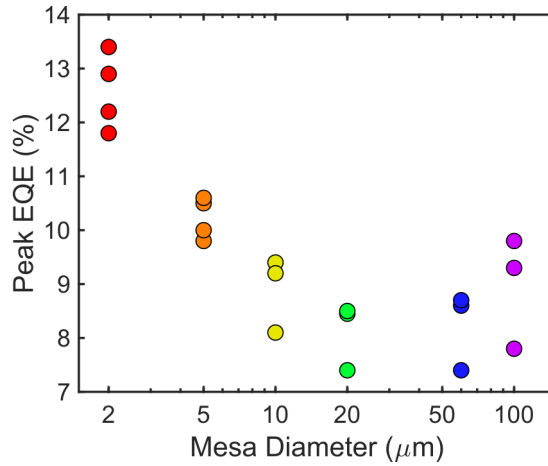
Figure 3.3: Peak EQE for different microLEDs. Multiple data points for each size represent different devices.

3.3   Optoelectronic characterization of microLEDs

In order to quantify the light output of an LED, the emitted photons must be collected and converted into an electrical signal. The simplest way to accomplish the task is to send to light into a photodiode, where a photon is absorbed by a semiconductor material to produce an electron-hole pair. The photo-generated carriers are transported to metal contacts to complete and electric circuit. This method of measuring light intensity, however, does not provide any information regarding the emission wavelength. Instead, a spectrometer can be used to separate light emission by wavelength diffraction optics. Light enters the spectrometer through a slit and is collimated by a parabolic mirror. The collimated light is directed towards a special diffraction grating (known as a blazed grating) that has been precisely machined sawtooth pattern that efficiently couples light into a single diffraction order. The wavelength components of an incident polychromatic beam, such as LED quantum well emission, will diffract at slightly different angles depending. An incident beam of light at an angle, θ_i, will diffract according to the grating
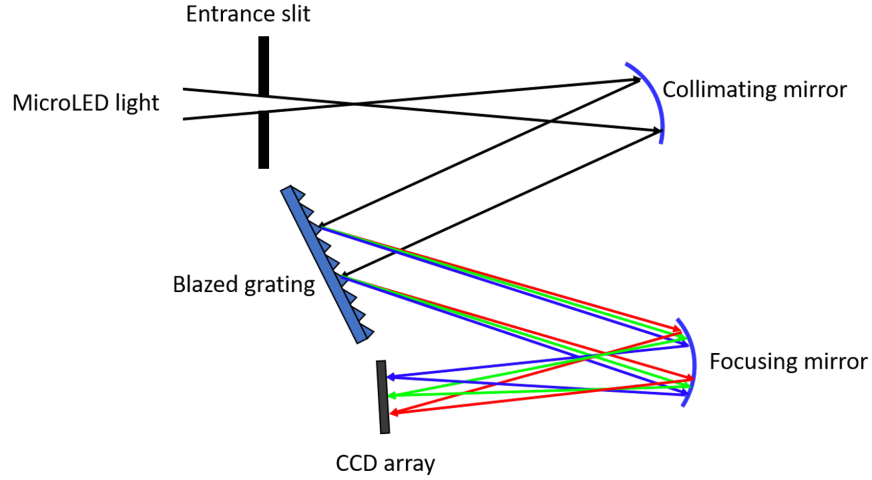
Figure 3.4: Schematic of the internal optical components of a spectrometer.

equation:

$$\theta_m = \sin^{-1}\left(\sin\theta_i - \frac{m\lambda}{d}\right) \tag{3.1}$$

where d is the spacing between sawtooth structures, m is the diffraction order, λ is the incident wavelength, and θ_m is the angle at which diffracted light has a maximum intensity. The separated wavelength components are then each focused onto different pixels on a charge-coupled device (CCD). The charges on each pixel are then binned and counted to produce light intensity as a function of pixel position, where the pixel position may be calibrated to a specific wavelength using a mercury-argon calibration source.

Next, the system must be radiometrically calibrated to convert arbitrary units of counts to Watts per nm. A NIST-traceable blackbody calibration source may be used that has a known output spectra in units of W/nm. After measuring the blackbody spectra in the spectrometer setup with the given collection optics, a calibration factor may be calculated by:

$$G(\lambda_g, \lambda) = \frac{I_{BB,ref}}{I_{BB,meas}} \tag{3.2}$$

where G is the calibration, or gain, factor, λ_g is the center diffracted wavelength of the
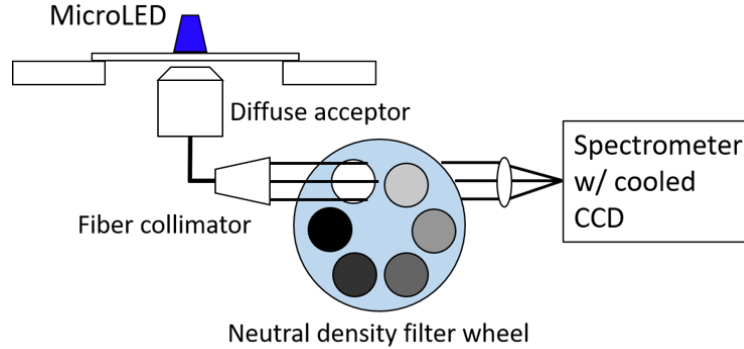
21

Figure 3.5: Schematic of the microLED testing system. Light is collected in the diffuse acceptor and coupled into a fiber optic cable. The light is output as a collimated beam and passes through a neutral density filter wheel (ND = 0, 0.5, 1, 2, 3, 4) and focused into a spectrometer with thermoelectrically cooled CCD.

grating position, λ is the light wavelength, $I_{BB,ref}$ is the calibrated reference blackbody spectrum, $I_{BB,meas}$ is the measured intensity from the blackbody source. After calculating the calibration factor, the measured electroluminescent intensity from an LED may be integrated to yield radiometric power by:

$$P_{out} = \int d\lambda \ I_{meas}(\lambda)G(\lambda_g, \lambda) \tag{3.3}$$

where $I_{meas}(\lambda)$ is the measured spectral intensity.

Backside emission electroluminescence (EL) measurements were conducted by sweeping current densities from 0.1 to 1000 A/cm^2 (60 and 100 μm devices were only tested up to 500 A/cm^2). Light was collected out the bottom of the substrate with a cosine corrector (Ocean Optics CC-3-DA) having an effective collection half angle of 60°. Light was transported via fiber optic and focused into a Horiba Jobin-Yvon iHR320 monochromator with a thermoelectrically cooled Synapse CCD detector. The optical system was calibrated using a radiometric blackbody source (Ocean Optics LS-1-CAL) to obtain the spectral flux in μW/nm. The peak wavelength, λ_p, was set as the centroid of the spectral flux and the power, P, was determined by integrating the flux. EQE curves were

calculated from optical measurements by

$$\text{EQE} = \frac{q}{hc}\frac{\lambda_p P}{I} \tag{3.4}$$

where I is the current, q is the fundamental electron charge, h is Planck's constant and c is the speed of light in vacuum.

3.4   Device results

Figure 3.2 shows current density-voltage characteristics of different LEDs with mesa diameters noted, where J is calculated using the area of the active region. Reverse bias leakage values out to -10 V were below the minimum detection limit of our instrument ($\sim$ 600 pA). Sidewall defects may act as current leakage pathways, [28, 29] and it has been shown that these conduction pathways may be closed through ALD passivation and chemical treatments.[23, 24] Above 2.5 - 3.0 V, high injection and ohmic resistance are responsible for deviations from exponential diode behavior.[30]

The peak EQE for different device sizes is shown in Fig. 3.3, and varies from 8-9% for large devices (100 μm mesa) to 12-13.5% for the smallest size (2 μm mesa). The 100, 60 and 20 μm microLEDs were nearly identical statistically, although the 100 μm devices exhibited slightly higher peak EQE values on average. Peak EQE values then rose sharply when the diameter was reduced from 20 to 2 μm. This effect is attributed to enhanced light extraction as more light reflects off the mesa sidewalls when the device diameter is reduced.[26]

The EQE trends in Fig. 3.3 may be better understood by considering the ABC model as follows:

$$\text{EQE} = \text{LEE} \times \frac{BN^2}{AN + BN^2 + CN^3} \tag{3.5}$$
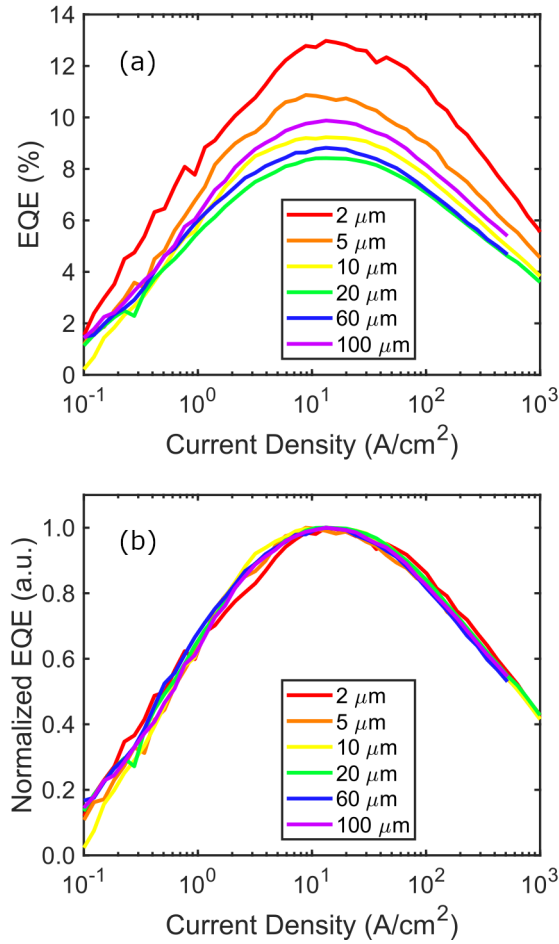
Figure 3.6: (a) EQE curves for different size microLEDs. In panel (b), the EQE curves are normalized to the respective peak EQE of the curve. Size annotations refer to the mesa diameter.

where LEE is the light extraction efficiency, N is the carrier density and A, B and C are the SRH, radiative and Auger recombination coefficients, respectively. The LEE is expected to be independent of J, except in large devices operating at current densities far above the peak current density, J_{peak}, where current-crowding effects begin to emerge. The carrier density and current density may be related by the following:

$$J = qw \left(AN + BN^2 + CN^3 \right) \tag{3.6}$$

where w is the thickness of the active region. The carrier density at the peak EQE (N_{peak}) may be found by differentiating Eq. (3.5) and setting the result equal to zero to obtain $N_{peak} = \sqrt{A/C}$. Substituting this into Eq. (3.6) yields:

$$J_{peak} = qw \left(2\frac{A^{3/2}}{C^{1/2}} + \frac{AB}{C} \right) \tag{3.7}$$

which relates J_{peak} to the ABC coefficients. The measured EQE curves for different devices as a function of J are shown in raw and normalized forms in Figs. 3.6(a) and 3.6(b), respectively. The EQE (following the general trend in Fig. 3.3) is clearly higher in the smallest devices, and moreover, all curves coincide when normalized in Fig. 3.6(b). The latter observation suggests that the ABC model coefficients are indeed size-independent, and therefore, that LEE is changing with device size. The measured J_{peak} values were 12.0, 13.7, 14.7, 14.0 15.3 and 14.6 for $d = 2$, 5, 10, 20, 60 and 100 μm, respectively. It is important to note that any changes in recombination coefficients would affect the shape of EQE curves as well as J_{peak}. Other factors that could influence the size-dependent EQE, such as device heating or current crowding, typically become more pronounced as the current density increased; these effects are also not expected to be strong in the size ranges where EQE changes the most (2-20 μm).[31] However, our EQE enhancement data are independent of current density, for which the only known explanations would be related to light extraction or optical collection efficiency.

Surface recombination losses are generally accepted to increase the A coefficient, which reduces the peak EQE and increases J_{peak}. Previous reports have shown that J_{peak} increases by a factor of 2 to 10 as the lateral mesa dimension is reduced, depending on the processing conditions and size ranges.[16, 18, 23] Here, the A coefficient is size-independent, meaning that SRH losses are dominated by bulk defects that nucleate during material growth. KOH will not etch away the (0001) plane, but will etch away

nonpolar and semipolar planes.[32] The plasma damaged sidewall is removed until the $\{10\bar{1}0\}$ planes are exposed, at which point, the etch rate slows down significantly.[22, 33] The exposed crystal planes are expected to have fewer defects than an etched surface, thus minimizing nonradiative surface recombination centers.[21] The semi-parabolic mesa structure is preserved after KOH etching since the facet sizes are significantly smaller than the mesa diameter, which is more compatible with chip shaping for light extraction engineering.[26, 34]

3.5 Light extraction modeling

3.5.1 Snell's law and total internal reflection (TIR)

When an electromagnetic wave encounters an interface between two mediums of different refractive indices, the energy is split into a transmitted wave and a reflected wave. At the interface of two dielectric mediums and a given angle of incidence, θ_i, and refractive indices n_1 and n_2, the angle of transmitted (i.e. refracted) wave may be determined by Snell's law:

$$n_1 \sin \theta_i = n_2 \sin \theta_t \tag{3.8}$$

where θ_t is the angle of the transmitted wave. At some critical angle, θ_c, the angle of the reflected light is 90°, which is given by:

$$\theta_c = \sin^{-1}\left(\frac{n_2}{n_1}\right) \tag{3.9}$$

This phenomenon is known as total internal reflection (TIR) where there is no transmitted wave component.

The amplitude of the reflected and transmitted waves (as well as their relative phases)

may be understood by considering the electric field. The incident, reflected and transmitted waves have the form:

$$E_i = E_{io}e^{i(\omega t - \boldsymbol{k_i} \cdot \boldsymbol{r})} \tag{3.10}$$

$$E_r = E_{ro}e^{i(\omega t - \boldsymbol{k_r} \cdot \boldsymbol{r})} \tag{3.11}$$

$$E_t = E_{to}e^{i(\omega t - \boldsymbol{k_t} \cdot \boldsymbol{r})} \tag{3.12}$$

where $\boldsymbol{r}$ is the position vector, and the $\boldsymbol{k}$ are the wave vectors. Electromagnetic field theory demands that the tangential components of the electric and magnetic fields at a boundary between two dielectric media must be continuous (assuming a relative magnetic permeability of $\mu_r = 1$). This provides the boundary conditions that $E_\perp(1) = E_\perp(2)$ and $B_\perp(1) = B_\perp(2)$ that may be applied at the dielectric interface to yield Fresnel's equations. Defining $n = n_2/n_1$, the reflection and transmission coefficients for $E_\perp$ are:

$$r_\perp = \frac{E_{r0,\perp}}{E_{i0,\perp}} = \frac{\cos\theta_i - \sqrt{n^2 - \sin^2\theta_i}}{\cos\theta_i + \sqrt{n^2 - \sin^2\theta_i}} \tag{3.13}$$

$$t_\perp = \frac{E_{t0,\perp}}{E_{i0,\perp}} = \frac{2\cos\theta_i}{\cos\theta_i + \sqrt{n^2 - \sin^2\theta_i}} \tag{3.14}$$

There are also corresponding reflection and transmission coefficients for the $E_\parallel$ fields:

$$r_\parallel = \frac{E_{r0,\parallel}}{E_{i0,\parallel}} = \frac{\sqrt{n^2 - \sin^2\theta_i} - n^2\cos\theta_i}{\sqrt{n^2 - \sin^2\theta_i} + n^2\cos\theta_i} \tag{3.15}$$

$$t_\parallel = \frac{E_{t0,\parallel}}{E_{i0,\parallel}} = \frac{2n\cos\theta_i}{n^2\cos\theta_i + \sqrt{n^2 - \sin^2\theta_i}} \tag{3.16}$$

The reflection and transmission components are related by the conservation of energy

$$r_\parallel + nt_\parallel = 1 \tag{3.17}$$

$$r_\perp + t_\perp = 1 \tag{3.18}$$

Using these coefficients, the reflectance coefficients are then calculated by:

$$R_\perp = |r_\perp|^2 \tag{3.19}$$

$$R_\parallel = |r_\parallel|^2 \tag{3.20}$$

where the overall reflectance, R, is simply the average between the two such that $R = \frac{1}{2}(R_\perp + R_\parallel)$. The transmittance coefficients are very similar, although one must consider that the transmitted wave is in a different medium:

$$T_\perp = \frac{n_2}{n_1} |t_\perp|^2 \tag{3.21}$$

$$T_\parallel = \frac{n_2}{n_1} |t_\parallel|^2 \tag{3.22}$$

Absorption effects in these coefficients is accounted for by simply using the complex refractive index, $N = n + i\kappa$, in place of the real refractive index.

3.5.2 Evanescent waves and optical tunneling

When the angle of incidence, θ_i exceeds the critical TIR angle, θ_c, all the light is reflected and there is no transmitted wave. According to the boundary conditions used in the development of the Fresnel equations, an electric field must exist in the forbidden medium 2. This electric field is part of what is called an evanescent wave, which has a
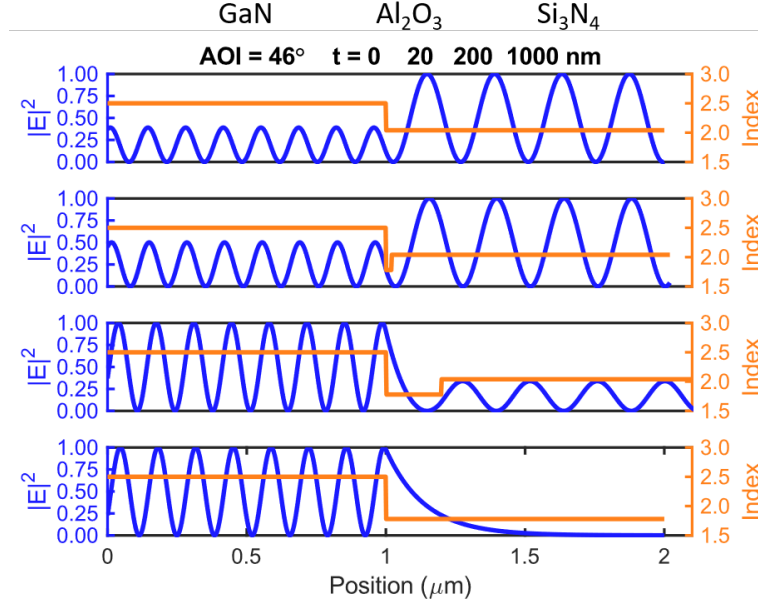
Figure 3.7: Electric field distributions in a $GaN/Al_2O_3/Si_3N_4$ dielectric stack. The Al_2O_3 layer ($n = 1.7$) thickness was varied from 0 to 1000 nm with an angle of incidence (AOI) of 46°, which exceeds the Snell's law TIR condition.

penetration depth, δ, according to:

$$\frac{1}{\delta} = \frac{2\pi n_2}{\lambda_0}\sqrt{\left(\frac{n_2}{n_1}\right)^2 \sin^2 \theta_i - 1} \tag{3.23}$$

where λ_0 is the free space wavelength. In the microLED device structure, there is a thin Al_2O_3 (20 nm) passivation layer and a much thicker Si_3N_4 insulation layer (250 nm). The evanescent field penetration depth into an Al_2O_3 layer is actually much longer than the layer thickness ($\delta \sim 100$ - 200 nm). Light that would normally undergo TIR at the Al_2O_3/GaN interface according to Snell's law may actually tunnel through via the evanescent field and transmit into the Si_3N_4 layer (see Fig. 3.7). The reflectance of this dielectric stack is almost entirely dominated by the refractive index contrast between the GaN and Si_3N_4 unless the Al_2O_3 layer is comparable to the evanescent field penetration depth.

The electric field in a GaN/Al$_2$O$_3$/Si$_3$N$_4$ stack was calculated through analytical transfer matrix methods in Fig. 3.7. The angle of incidence (AOI) is set to 46°, which is greater than the Snell's law critical angle for TIR. At $t_{AlO} = 0$ nm (when no Al$_2$O$_3$ layer exists) and when $t_{AlO} = 20$ nm, the electric field distributions are nearly identical. As t_{AlO} increases to 200 nm, the field intensity decays in the Al$_2$O$_3$ layer but still partially transmits into the Si$_3$N$_4$. When $t_{AlO} \gg \delta$, the field completely decays and experiences TIR.

3.5.3 Modeling quantum well emission

Transitions between the conduction band and each valence band generates light via dipole radiation. The associated dipole radiation profile for each band is as follows:

$$\text{HH}: I_x = \sin^2\theta\sin^2\phi + \cos^2\theta \tag{3.24}$$

$$\text{LH}: I_y = \sin^2\theta\cos^2\phi + \cos^2\theta \tag{3.25}$$

$$\text{CH}: I_z = \sin^2\theta \tag{3.26}$$

The three valence bands are the light hole band (LH), heavy hole band (HH) and the crystal field split off band (CH). The crystal field split off energy, Δ_{cr} is about 0.04 eV, which is large enough for transitions in this energy band to be improbable ($\Delta_{cr} > kT = 0.026$ eV). The aggregate emission profile is the sum of the HH and LH dipoles

$$I(\theta) = \sin^2\theta\sin^2\phi + \sin^2\theta\cos^2\phi + 2\cos^2\theta \tag{3.27}$$

$$= \sin^2\theta\left(\sin^2\phi + \cos^2\phi\right) + 2\cos^2\theta \tag{3.28}$$
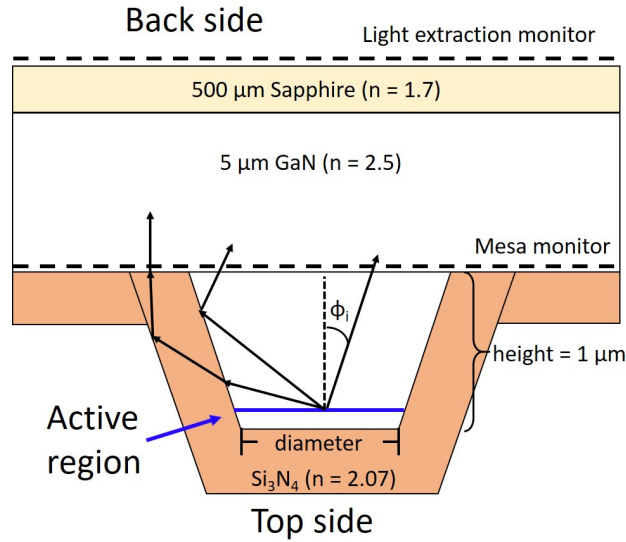
$$= 1 + \cos^2\theta \tag{3.29}$$

Figure 3.8: Schematic of ray tracing model showing the main light propagation regimes. Light propagates at an initial angle of ϕ_i from normal.

This function then becomes the initial angular trajectory distribution for light emission during extraction modeling.

3.6 Ray tracing modeling of microLEDs

To assess how LEE might change with device size, Monte Carlo ray tracing studies were conducted using the commercial software package Synopsys LightTools, as outlined in Fig. 3.8. The model consisted of a 1 μm tall truncated pyramid GaN ($n = 2.5$) mesa structure with a sidewall angle of 25° from vertical. The top of the mesa was a partially absorbing mirror with an 87% reflectance (i.e. as calculated for an Si_3N_4/Al interface via Fresnel reflection and averaged over 0-90°) and a diameter of 2, 5, 10, 20, 60 or 100 μm. A 250 nm Si_3N_4 ($n = 2.07$) layer covered the entire mesa where the outer surface was a mirror with an 87% reflectance. The 20 nm Al_2O_3 passivation layer was omitted from the ray-tracing model since it would have a negligible effect on the

31

GaN/Si$_3$N$_4$ reflectance[1] (i.e. the evanescent field penetration depth is far greater than the Al$_2$O$_3$ layer thickness).[35] The mesa was sitting on a 5 μm GaN layer and a 500 μm sapphire substrate layer, and the angular distribution of emitted light from the mesa was calculated as well as the light extraction out the bottom of the sapphire substrate. The quantum well emission was modeled as a 10 nm thick non-ray-traceable volumetric source where 10 million monochromatic rays (λ = 465 nm) were generated with a uniformly distributed initial position out to the mesa edge. The initial ray propagation direction, ϕ_i, has azimuthal symmetry, while the polar direction was weighted by $1 + \cos^2 \phi_i$ due to GaN valence band characteristics.[36] The backside LEE and emission profile into air in Figs. 3.9(a)-(b) were calculated at the "Light extraction monitor" plane in Fig. 3.8, and the angular emission profiles were calculated at both the "Mesa monitor" and "Light extraction monitor" planes. The sapphire/air interface was modeled as rough (an ideal Lambertian scattering profile) as well as a perfectly perfectly smooth surface to evaluate the importance of surface roughness. The real scattering profile is expected to lie between these two extreme cases.

The calculated angular emission profiles from the sapphire backside into air are shown in Figs. 3.9(a)-(b). The emission intensity for both cases increases for all angles as the mesa diameter decreases, qualitatively following the measured peak EQE trends. The backside LEEs for the rough sapphire are [64.5, 48.8, 41.2, 37.4, 34.7, 34.0]% for d = [2, 5, 10, 20, 60, 100] μm, respectively. The smooth backside LEE values–which have approximately the same diameter-dependent enhancement–are [25.1, 17.0, 14.1, 12.9, 12.3, 12.2]% for the same geometries. This suggests that the sapphire roughness determines the overall LEE magnitude but is not responsible for the diameter-dependence; that effect is attributed to internal reflections at the mesa sidewall. The calculated angular

---

[1]Analytical transfer matrix calculations with the Lumerical STACK package were carried out to confirm the validity of neglecting the 20 nm thick Al$_2$O$_3$ layer.
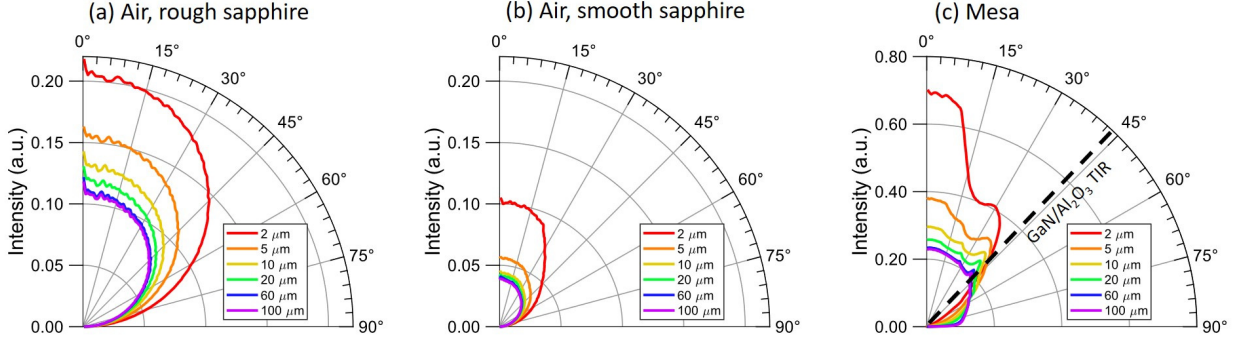
Figure 3.9: Angular emission profiles calculated at the (a)-(b) "Light extraction monitor" plane and the (c) "Mesa monitor" plane. The angle normal to the mesa bottom is defined as $\phi = 0°$. The dashed line in (c) corresponds to the critical angle for TIR at the GaN/sapphire interface.

emission profile at the "Mesa monitor" plane in Fig. 3.9(c) shows increased directionality of light propagation from smaller mesas. Rays initialized with trajectories beyond the critical angle ($\phi_{crit} \sim 45°$) that reflect off the inclined mesa sidewall are redirected closer to normal, thus reducing TIR losses. In smaller diameter mesas, rays are generally much closer to the sidewall, and consequently more sidewall reflections occur. All in all, these simulations confirm that LEE can indeed change as device dimensions decrease, which is borne out in the measured EQE trends and size-independent ABC coefficients.

3.7   Conclusion

In this work, KOH etching and Al_2O_3 dielectric passivation were used to minimize the effect of nonradiative sidewall defects in InGaN/GaN microLEDs with mesa diameters ranging from 100 to 2 μm. The peak EQE of devices was seen to increase from $\sim 9\%$ to $\sim 13\%$ as the device diameter was decreased from 100 to 2 μm, which was attributed to enhanced backside light extraction efficiency. Moreover, EQE curve trends at 0.1-1000 A/cm^2 exhibited constant ABC model coefficients, suggesting size-independent internal efficiency down to 2 μm diameter devices. Ray tracing simulations determined

that reducing the mesa diameter increased directionality–leading to fewer TIR losses in the substrate–thus confirming the experimental trend of higher EQE for small devices. Overall, this work suggests that nonradiative losses in microLEDs could potentially be minimized with appropriate processing, and the efficiency losses in ultrasmall devices required for next-generation displays may be overcome in blue InGaN microLEDs.

Chapter 4

Strain relaxation by post-growth top-down patterning

Portions of this chapter have been adapted from [37]

4.1 Introduction

Nanopatterning the active region of InGaN-based LEDs, using techniques such as self-assembled Ni nanoisland [38, 39] or SiO_2 (colloidal crystal) etch masks,[40–48] as well as nanoimprint,[49] interference [50, 51] and electron beam lithographies,[52] is a potential route to alleviate some strain-related issues in the nitride material system. These approaches have largely been used for light extraction engineering and to create photonic crystals, but there are indications that nanopatterning could indeed relieve material strain. For example, Wang *et al.* reported a current-independent blueshift in electroluminescence (EL) emission from InGaN/GaN nanorods (50-100 nm), as compared to planar films, suggesting that piezoelectric fields were reduced upon nanopatterning.[45] In other work, Wu *et al.* studied the influence of nanorod diameter through photolumi-

nescence (PL)[38]; the authors found that the PL peak energy increased with decreasing diameter, and they attributed this observation to reduced QCSE resulting from strain relaxation. Keller *et al.* also conducted power-dependent PL measurements on planar and nanopatterned InGaN/GaN multi-quantum wells (MQWs) and found the emission energy to increase with pump power for both cases. In these latter measurements, photo-generated carriers were thought to screen piezoelectric fields (and the QCSE)[53], making it difficult to independently determine strain state. Size-dependent effects in the nitrides have also been studied using continuous/time-resolved PL and Raman spectroscopy [52–55], but these works did not directly determine strain state as a function of size.

X-ray diffraction (XRD), on the other hand, can be used to directly determine the strain state of a material [56]. Previous XRD studies of nanopattered InGaN/GaN MQWs have only considered one size or different In compositions within a specific experiment [50, 51, 57, 58], and they have not investigated if strain relaxation is size dependent. Moreover, the importance of an potential for nanopatterning to reduce strain in the III-nitrides, as evidence by direct measurement and correlation of strain state with emission characteristics for different feature sizes, has not been investigated. In the present study, InGaN/GaN MQWs were characterized by XRD before and after nanopatterning (e.g. nanorod diameters from 120-900 nm) using reciprocal space mapping (RSM) and further characterized using power-dependent PL to correlate strain relaxation with PL energy shifts. In all cases, sub-micron scale lateral patterning of MQW emitters resulted in significant strain relaxation (15-32%) and blue-shifted emission that increased with the degree of relaxation and excitation power.

4.2   Polarization in III-nitrides

The nitrides are hexagonal wurtzite crystals (Fig. 4.1), which give rise to large polar-
ization fields due to the lack of inversion symmetry and the ionic nature of the (Al, Ga,
In)-N bond. Furthermore, strained epitaxial layers, such as InGaN/GaN heterostruc-
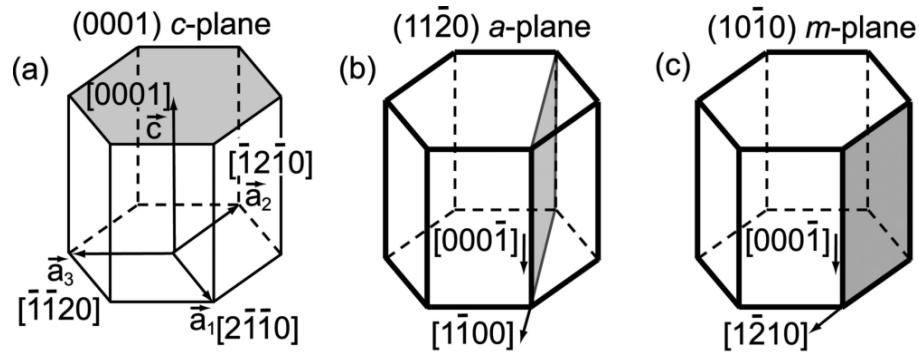

Figure 4.1: Common crystal planes of hexagonal unit cells.

tures, have a deformed crystal structure that also generates a piezoelectric polarization
field. The piezoelectric component adds to the equilibrium polarization, more commonly
referred to as the spontaneous polarization field. When the polarization field changes
between adjacent epitaxial layers, sheet charges build up at the interface. The polariza-
tion field differences and sheet charges are very large in GaN/InGaN/GaN quantum well
double heterostructures. The sheet charges on both sides of the InGaN quantum well
establish an electric field that bends the conduction band and valence band, thus forcing
electrons and holes apart to opposite sides of the well. Known as the quantum-confined
Stark effect (QCSE), this effect lowers the radiative efficiency and lengthens the radiative
lifetime. The radiative recombination coefficient, B, is proportional to the square of the
electron-hole wavefunction overlap; it has also been shown that the Shockley-Read-Hall
and Auger recombination rates scale with the square of the electron-hole wavefunction
overlap[59].

37

4.3   Stress and strain relations

Stress and strain in crystals can be generalized by the following relation:

$$
\begin{bmatrix} \sigma_{xx} \\ \sigma_{yy} \\ \sigma_{zz} \\ \sigma_{xy} \\ \sigma_{xz} \\ \sigma_{yz} \end{bmatrix} = \begin{bmatrix} C_{11} & C_{12} & C_{13} & 0 & 0 & 0 \\ C_{12} & C_{11} & C_{13} & 0 & 0 & 0 \\ C_{13} & C_{13} & C_{33} & 0 & 0 & 0 \\ 0 & 0 & 0 & C_{44} & 0 & 0 \\ 0 & 0 & 0 & 0 & C_{44} & 0 \\ 0 & 0 & 0 & 0 & 0 & \frac{C_{11}+C_{12}}{2} \end{bmatrix} \begin{bmatrix} \epsilon_{xx} \\ \epsilon_{yy} \\ \epsilon_{zz} \\ \epsilon_{xy} \\ \epsilon_{xz} \\ \epsilon_{yz} \end{bmatrix}
\tag{4.1}
$$

where σ_{ij} is stress, C_{ij} is the elastic stiffness tensor and ϵ_{ij} is strain. In [0001] oriented InGaN/GaN films, there are no shear stresses ($\sigma_{i\neq j}$ and $\sigma_{i\neq j} = 0$) and the film has *isotropic biaxial* strain ($\epsilon_{xx} = \epsilon_{yy} = \epsilon_\parallel$ and $\epsilon_{zz} = \epsilon_\perp$). Biaxial strain also means there is no out-of-plane stress but there is out-of-plane strain. With these simplifications, Eq. (4.1) simplifies to

$$
\begin{bmatrix} \sigma_\parallel \\ \sigma_\parallel \\ 0 \end{bmatrix} = \begin{bmatrix} C_{11} & C_{12} & C_{13} \\ C_{12} & C_{11} & C_{13} \\ C_{13} & C_{13} & C_{33} \end{bmatrix} \begin{bmatrix} \epsilon_\parallel \\ \epsilon_\parallel \\ \epsilon_\perp \end{bmatrix}
\tag{4.2}
$$

$$
\epsilon_\parallel = \frac{a_{\text{meas}}^{\text{InGaN}} - a_0^{\text{InGaN}}(x)}{a_0^{\text{InGaN}}(x)}
\tag{4.3}
$$

$$
\epsilon_\perp = \frac{c_{\text{meas}}^{\text{InGaN}} - c_0^{\text{InGaN}}(x)}{c_0^{\text{InGaN}}(x)}
\tag{4.4}
$$

where $a_{\text{meas}}^{\text{InGaN}}$ is determined from an XRD measurement and a_0^{InGaN} is linearly interpolated from Vegard's Law by $a_0^{\text{InGaN}}(x) = xa_0^{\text{InN}} + (1-x)a_0^{\text{GaN}}$. Setting $\sigma_\perp = 0$ in Eq. (4.2), one may relate the in-plane and out-of-plane strain by:

$$
\epsilon_\perp = -2\frac{C_{13}(x)}{C_{33}(x)}\epsilon_\parallel
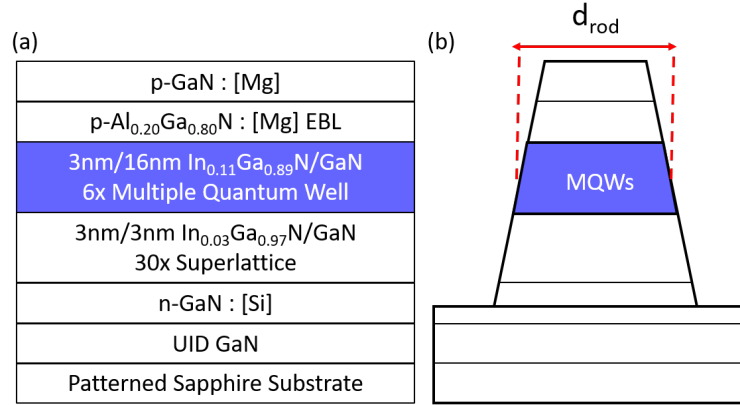\tag{4.5}
$$

Figure 4.2: (a) Schematic of the epitaxial structure grown by MOCVD and (b) geometry of the etched nanopatterned material.

which provides a nonlinear algebraic equation that is solved for the composition. Eq. (4.5) requires experimental inputs for the GaN and InGaN lattice constants in order to solve the equation. In my work, these lattice constants will be measured by x-ray diffraction, which will allow for determination of both strain and composition.

4.4   X-ray diffraction reciprocal space mapping

InGaN/GaN samples were grown on [0001]-oriented patterned sapphire substrates by metal-organic chemical vapor deposition (MOCVD), as summarized in Fig. 4.2. The growth consisted of a 1.4 μm unintentionally doped (UID) GaN layer, 4 μm Si-doped n-type layer, and 30 period Si-doped $In_{0.03}Ga_{0.97}N$/GaN superlattice with a 20 nm UID GaN cap. The active region consisted of 6 periods of a 3 nm $In_{0.11}Ga_{0.89}N$ quantum well with 16 nm thick GaN barriers capped with a Mg-doped p-$AlGa_{0.20}Ga_{0.80}$ electron blocking layer (EBL) and a 120 nm thick Mg-doped p-type layer.

The epitaxial device structure above was grown on a single sapphire wafer, cut into four separate planar samples, and subsequently nanopatterned using a colloidal lithography process that has been described in detail elsewhere [60]. Silica colloids (d =

170, 310, 690, 960 nm) were functionalized (allytrimethoxysilane) and deposited using a Langmuir-Blodgett dip coating process, leaving behind a hexagonally close-packed mono-layer "mask" on the surface. Samples were dry etched in a Cl_2/N_2 inductively-coupled plasma (ICP) to fabricate the nanostructures. Colloid size largely determined the final diameter (d_{rod}) of the InGaN features; a small amount of sidewall slope was present due to mask shrinkage during the etching process. Each sample, one for each nanorod diameter, was fully characterized both before (the "planar" state) and after nanopatterning. X-ray diffraction measurements were performed on a Panalytical MRD Pro with a 3D Pixcel detector using monochromated CuKα radiation ($\lambda = 1.5405$ Å). Reciprocal space maps (RSMs, 2θ scans for different ω) were taken along two asymmetric reflections, ($10\bar{1}5$) and ($11\bar{2}4$), and one symmetric reflection, (0002). Symmetric (0002) RSMs (via $\Delta\theta_{meas}$) were used to determine the c lattice constants and composition (x, In$_x$Ga$_{1-x}$N) of samples via the differential form of Bragg's law as follows [61, 62]:

$$\frac{\Delta d}{d_{ref}} = -\Delta\theta_{meas} \cot\theta_{ref} \tag{4.6}$$

The reference angle, θ_{ref} was determined via Bragg's law from the $hkil$ d-spacing using the a and c lattice constants of GaN and the standard quadratic form of a hexagonal lattice:

$$\frac{1}{d^2} = \frac{4}{3}\frac{h^2 + hk + k^2}{a^2} + \frac{l^2}{c^2} \tag{4.7}$$

where a and c are the theoretical constants constants of GaN [62]. The measured a constants of GaN and InGaN were determined by reciprocal space mapping analysis according to [56, 63, 64] the following:

$$Q_x^{hkil} = \frac{\cos\omega - \cos 2(\theta - \omega)}{\lambda} \tag{4.8}$$

$$Q_y^{hkil} = \frac{\sin \omega + \sin (2\theta - \omega)}{\lambda} \tag{4.9}$$

where ω and 2θ were the angles of the incident and diffracted beams measured from the surface and from the projected incident beam, respectively. Q_x and Q_y are the reciprocal lattice vectors of specific ($hkil$) planes. Other sources in the literature use $2\pi/\lambda$ instead of $1/\lambda$ for the Ewald's sphere diameter [64], but this would not affect the calculated d_{hkil} or lattice constants. For symmetric scans, the Q_x component should be exactly zero for c-plane GaN as epitaxial tilt is not present in this system. Any nonzero values for Q_x are attributed to the sample itself not being perfectly flat on the stage during the x-ray experiments. The effect of the true reciprocal lattice points can be seen in the figure below from Panalytical.
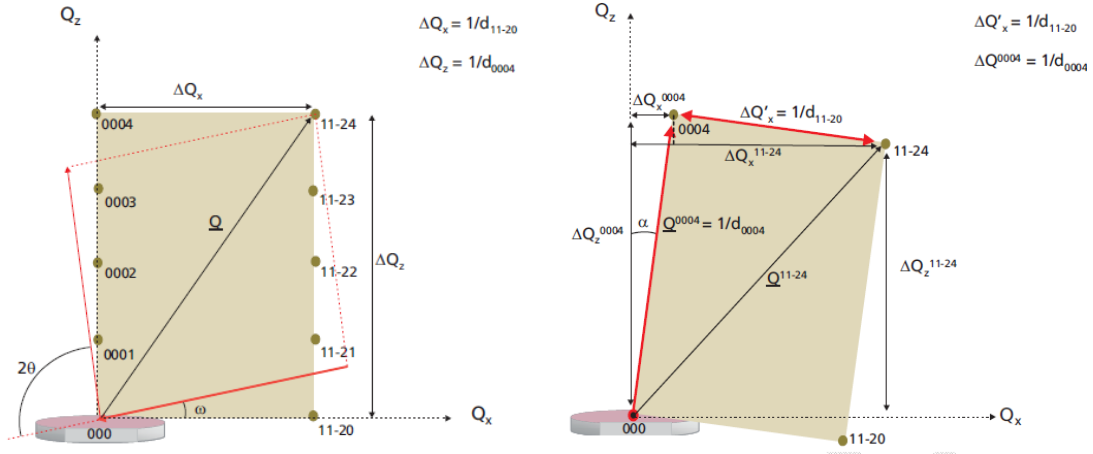

Figure 4.3: Reciprocal space for a perfectly flat sample (left) and a tilted sample (right)

To account for this, the sample tilt angle, α, is calculated by

$$\alpha = \tan^{-1} \left(\frac{Q_x^{0002}}{Q_z^{0002}} \right) \tag{4.10}$$

and the reciprocal space coordinates are rotated about α by the following:

$$\begin{pmatrix} Q_x \\ Q_z \end{pmatrix}_{\text{corrected}} = \begin{pmatrix} \cos\alpha & -\sin\alpha \\ \sin\alpha & \cos\alpha \end{pmatrix} \begin{pmatrix} Q_x \\ Q_z \end{pmatrix}_{\text{measured}} \tag{4.11}$$

The tilt corrected reciprocal lattice points are then used to determine the lattice constants.

$$Q_x = 1/d_{hki0} \tag{4.12}$$

$$Q_z = 1/d_{000l} \tag{4.13}$$

Using the a constants of GaN and $In_xGa_{1-x}N$, as well as the indium composition, x, the degree of relaxation is defined as:

$$R = \frac{a_{meas}^{InGaN} - a_{meas}^{GaN}}{a_{ref}^{InGaN}(x) - a_{ref}^{GaN}} \tag{4.14}$$

PL measurements were performed at 14 K with a 405 nm continuous-wave InGaN laser with power outputs up to 400 mW. Prior temperature studies found a negligible effect between measurements at room temperature and at 20 K [38]. The laser source was well above the bandgap of GaN (365 nm at room temperature and an estimated 353 nm at 20 K) so that carriers were only generated in the InGaN quantum wells. The beam was incident upon the sample at 45°, and emission was collected normal to the sample surface with a high numerical aperture collector and transported via fiber to a UV-Vis spectrometer (Ocean Optics USB2000+) to record the full PL spectrum at different laser pump powers. Peak wavelengths of spectra were extracted via Gaussian fit.

Scanning electron microscope (SEM) images of the colloidal mask deposition and nanostructured material after plasma etching are shown in Fig. 4.4. After etching, the

(a) $d_{colloid}$ = 960 nm   (b) $d_{colloid}$ = 690 nm   (c) $d_{colloid}$ = 310 nm   (d) $d_{colloid}$ = 170 nm

5 µm   2 µm   2 µm   2 µm

(e) d_{rod} = 900 nm   (f) d_{rod} = 600 nm   (g) d_{rod} = 250 nm   (h) d_{rod} = 120 nm
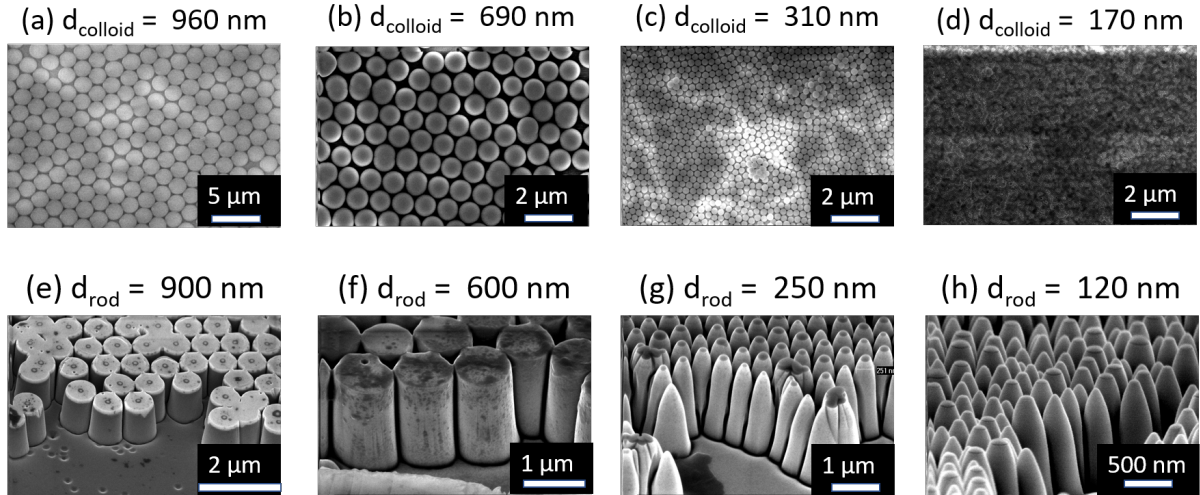
2 µm   1 µm   1 µm   500 nm

Figure 4.4: Scanning electron microscope (SEM) images of colloidal mask depositions (a-d) and the resulting nanopatterned materials after plasma etching (e-h).

diameter of the nanorods near the active region (about 100 nm below the top) were measured via SEM to be d_{rod} = 120, 250, 600, 900 nm. Imperfections in the hexagonally close-packed lattice were present, but did not contribute to the strain state of the active region.

Figure 4.5 shows a set of four RSMs for a single planar (unpatterned) sample that were use to characterize the initial strain state. The peak centroids were used to determine the lattice constants as well as indium composition of $In_xGa_{1-x}N$ using the (0002) reflections, i.e., for samples A-D, x was determined to be 0.11, 0.12, 0.12 and 0.10, respectively.

The a and c lattice constants for each sample were calculated from the asymmetric $(10\bar{1}5)$ and $(11\bar{2}4)$ RSMs and symmetric (0002) RSMs, respectively. These results are summarized in Section 4.4. Note that each of the measured GaN lattice constants had less than 1% deviation from the theoretical GaN lattice constant. The overall degree of relaxation, R from Eq. (4.14), was calculated from the $(10\bar{1}5)$ and $(11\bar{2}4)$ RSM reflections and averaged for each sample (A, B, C, D $\rightarrow$ 900, 600, 250, 120 nm nanopatterns, respectively), and the error represents the standard deviation between the two directions.
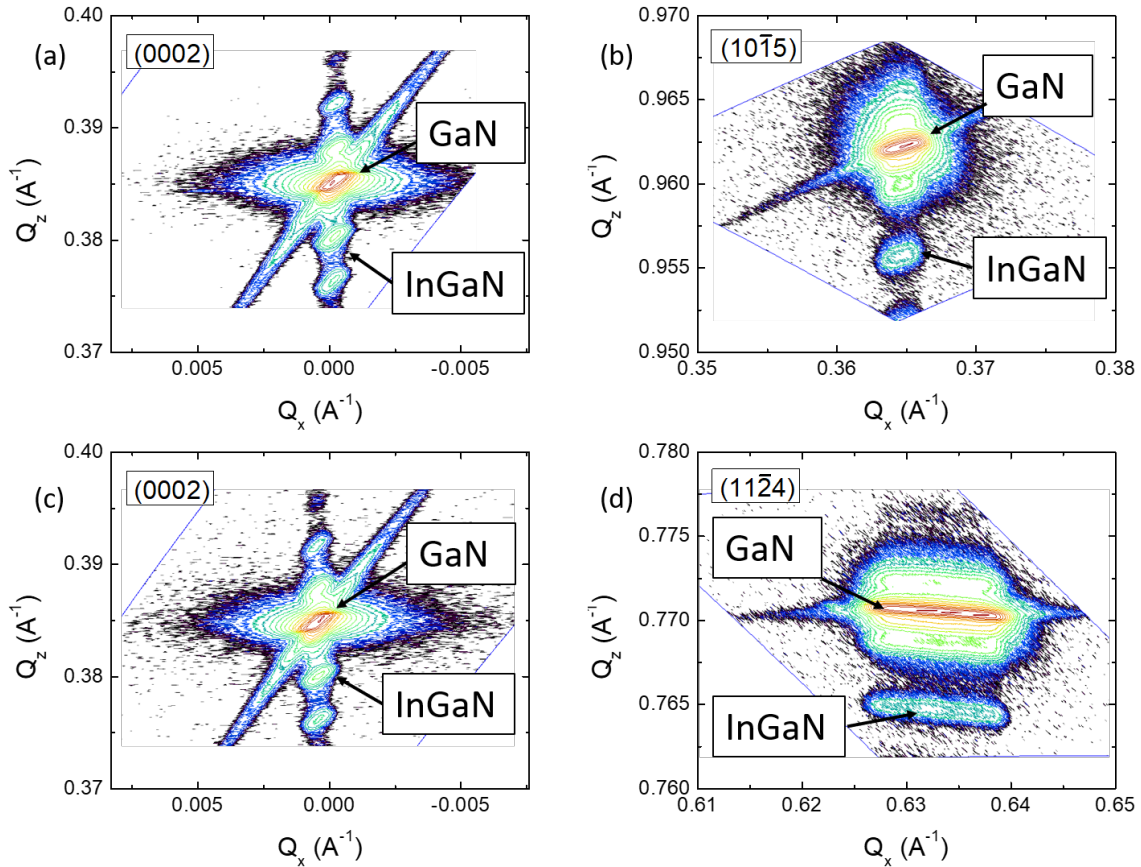
Figure 4.5: On (a),(c) and off-axis (b),(d) RSMs of a planar InGaN/GaN MQW sample. The (0002) RSMs in (a) and (c) were measured with the same stage angles (around [0002]) as the off-axis RSMs in (b) and (d), respectively. In some scans, higher order superlattice fringes appear below/above the InGaN or GaN peaks. The large diffuse streak is due to the x-ray monochromator divergence (i.e., parallel to the 2θ direction), and the peak broadening in panel (d) is due to a large x-ray spot on the sample at grazing incidence ($\omega \sim 11°$ and near normal takeoff for $2\theta \sim 100°$). Units are inverse Angstroms (Å^{-1}).

The relaxed In$_x$Ga$_{1-x}$N lattice constants were interpolated from Vegard's law to calculate the R values. After nanopatterning, the composition was held constant for the calculations of the relaxed InGaN lattice parameter. The measured GaN lattice constants after nanopatterning remain statistically equivalent.

Figure 4.6 shows example RSM data for planar versus nanopatterned samples. These data are summarized in Section 4.4, and indicate that R clearly depends on nanorod
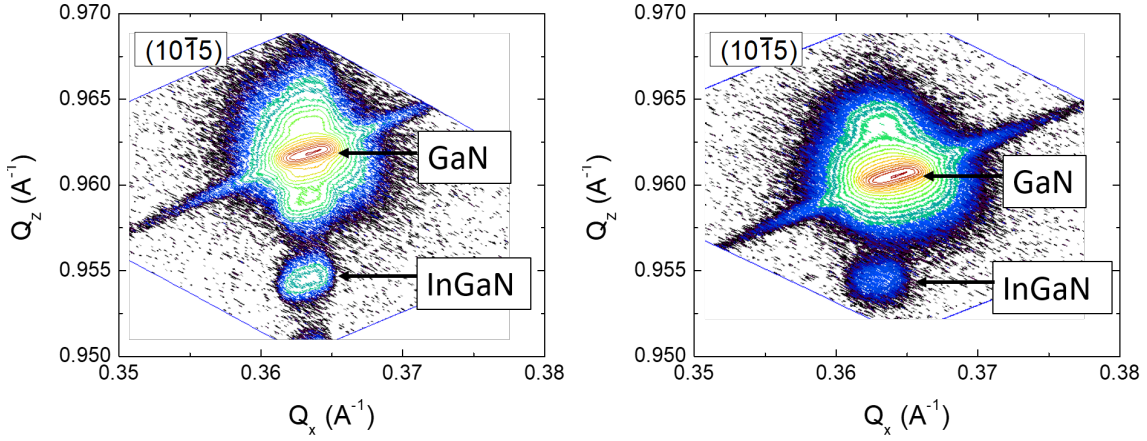
Figure 4.6: Example reciprocal space maps for (a) planar and (b) patterned ($d_{rod} =$ 250 nm) InGaN/GaN MQW samples, with a summary of strain relaxation values (R) shown in (c). R values calculated from different reflections were averaged with the standard deviation representing the error bar. Diameter (of the rod) refers to the location of the active well region.

diameter, and that nanopatterining results in significant strain relaxation for the range

of diameters considered. R increased as the diameter of the nanorod decreased, which

provides quantitative support for prior optical studies [38, 52] where strain relaxation

Table 4.1: Measured a and c lattice constants of GaN and InGaN for each sample (A-D), in planar and nanopatterned forms. Lattice constant values are listed in Angstroms. The (0002) scan was rotated 90° from (0002).

| Diameter	(10$\bar{1}$5) GaN	InGaN	(11$\bar{2}$4) GaN	InGaN	(0002) GaN	InGaN	(0002) GaN	InGaN
Planar A	3.183	3.185	3.188	3.188	5.198	5.290	5.197	5.289
Planar B	3.183	3.185	3.185	3.185	5.191	5.283	5.191	5.283
Planar C	3.180	3.180	3.190	3.190	5.194	5.287	5.194	5.287
Planar D	3.180	3.180	3.181	3.182	5.175	5.176	5.175	5.260
900 nm	3.192	3.198	3.188	3.192	5.196	5.284	5.196	5.286
600 nm	3.190	3.198	3.182	3.190	5.195	5.281	5.195	5.280
250 nm	3.180	3.191	3.185	3.197	5.191	5.274	5.191	5.276
120 nm	3.188	3.198	3.185	3.197	5.196	5.274	5.196	5.276
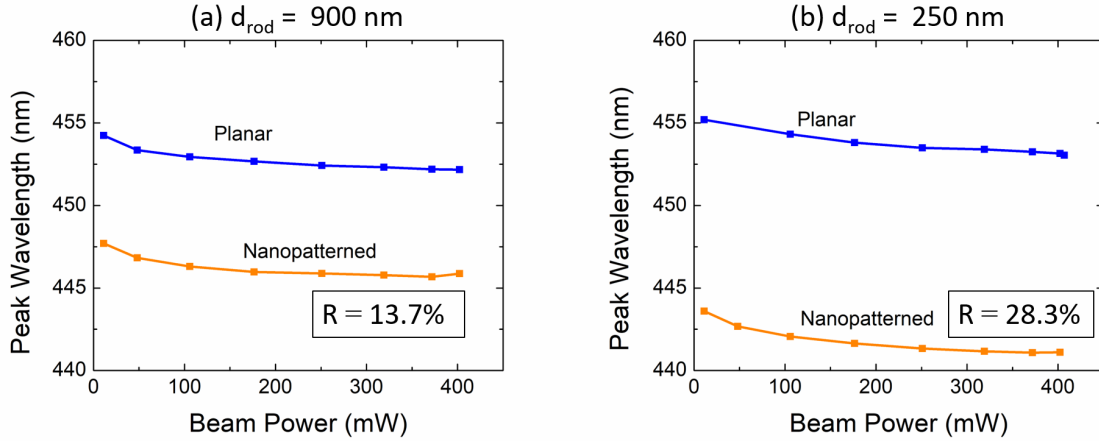
Figure 4.7: Peak wavelength of PL emission at 13 K from planar and patterned InGaN/GaN MQW structures for different excitation power densities at 405 nm.

was inferred. It should be noted that while R appeared to increase roughly linearly, it is entirely possible that nonlinearities exist outside the range of sizes tested here. Since pixel dimensions for advanced, near-eye display applications are likely to be ≤ 1 μm in the lateral dimension, larger sizes were not explicitly studied. Further reduction of the nanostructured diameter would require more advanced lithography techniques, and, additionally, any benefits of strain relaxation would likely be negated by sidewall defects introduced during plasma etching [16, 17, 65, 66].

4.5   Photoluminescence measurements

Two of the aforementioned samples were further characterized using power-dependent, low temperature PL at 14 K (Fig. 4.7) to assess the effect of strain relaxation on optical properties. Peak wavelengths were generally seen to blueshift with increasing excitation density, which is likely due to screening of the field by carriers [67]. Direct comparison of PL emission intensity, as a function of carrier density, is not realistically possible without exact knowledge of complex optical phenomena occurring in both nanopatterned and
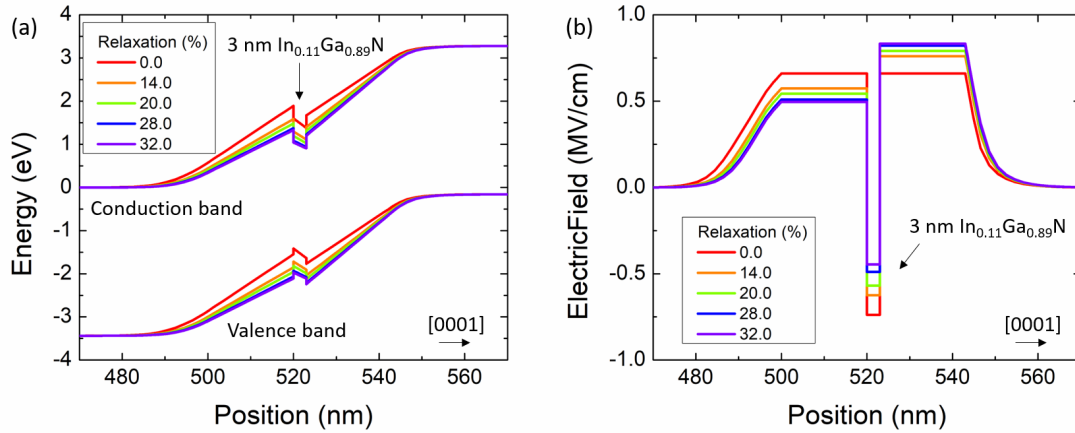
Figure 4.8: (a) Simulated energy band diagram and (b) electric field profiles for a single 3 nm InGaN quantum well (see text for details) with different degrees of in-plane relaxation from 0-32%. Relaxation values were chosen to represent the experimental values determined by XRD RSMs. The position axis, referenced to the substrate position, lies along the [0001] growth direction with only the active region displayed. Inset in (a) shows a zoom of the conduction band, where lower band tilt can be seen for greater relaxation.

planar material [44]. For example, one needs to consider the reflection and scattering processes at the GaN-air interface, pump light recycling, and fill factor of the nanopatterned material. Notwithstanding, the laser pump power was varied from 10–400 mW to qualitatively compare structures having reflectivity differences and (potentially) pump recycling effects. The planar samples exhibited nearly identical power-dependent PL curves, and, within the range of pump powers tested, nanopatterned sample PL was always blue-shifted. Moreover, the 250 nm nanorods had a more pronounced blue-shift effect, compared to the 900 nm nanorods, supporting the claim that more strain relaxation leads to more blue-shifted emission.

Poisson-Schrödinger simulations were also performed for a simplified single quantum well (SQW) structure using SiLENSe. The active region thickness was kept constant with thicker UID GaN barrier layers. The simulated structures consisted of 500 nm Si-doped n-GaN, 20 nm UID GaN barrier, 3 nm $In_{0.11}Ga_{0.89}N$ quantum well, 20 nm UID GaN

barrier and a 150 nm Mg-doped p-GaN capping layer. The degree of relaxation (R) in the InGaN quantum well was varied from 0-32% following the experimentally determined strain states from XRD. Figure 4.8 shows the calculated energy band diagram and electric field distribution of the SQW structure for each relaxation case under no applied bias. Increasing the degree of relaxation from 0 to 32% flattens out the energy bands in the 3 nm InGaN quantum well. This effect is attributed to a reduction in the piezoelectric field due to InGaN/GaN lattice strain, as shown in Fig. 4.8.

4.6 Conclusion

InGaN/GaN MQW samples were nanopatterned using a colloidal lithography and plasma etching process. The diameters of the final structures around the active region spanned an entire order of magnitude in length scale (120-900 nm), and RSM analysis before and after nanopatterning confirmed that in-plane strain was indeed relaxed after patterning. Moreover, smaller diameter features showed larger and larger strain relaxation (up to 32 %), which correlated well with the level of blueshift in PL. Complementary power-dependent PL measurements on the exact structures studied by RSM supported prior claims correlating strain relaxation and blue-shifting while minimizing the influence of carrier screening, pump recycling and differences in the surface relectivity. These trends are further supported with Poisson-Schrödinger simulations, demonstrating that relaxation decreases the internal piezoelectric field, leading to blue-shift in emission spectra.

Chapter 5

Towards electrically-injected sub-micron LEDs

5.1   Introduction

Both the fabrication and testing of nanoscale InGaN LEDs is very difficult. Not only is very high resolution lithography required, but also the devices may only be emitting power on the order of picowatts or even femotowatts. As a result, reports on nanoscale LEDs have predominantly been on arrays of LEDs rather than individual ones. The LED arrays are often planarized, using materials such as spin-on-glass (SOG), and then treating the array of LEDs as single large device where all the LEDs are connected in parallel. The fabrication processes are difficult and fluctuations between individual device properties within an array can make data analysis especially complicated. Moreover, open and short-circuit LEDs can prevent even a reasonable estimation of the average current density across the array of LEDs.

In 2016, Zhang *et al.* fabricated individually addressable nanowire LEDs with diameters using a top-down etch process with electron beam lithography.[68] Following the

mesa etch, the mesas were subjected to a 90 °C KOH treatment where the final diameter was about 270 nm. The presence of strain relaxation was observed through Raman spectroscopy by examining the shift in the E_2^h phonon peak of InGaN. The measured EL peak wavelength of the finished device was nearly constant as a function of current (blueshifting from 543.2 nm to 542.7 nm from 57.6 A/cm^2 to 1100 A/cm^2). Strangely, the peak wavelength was actually *red-shifted* in comparison to a planar LED (300 x 300 μm^2) processed from the same wafer–a phenomenon that is completely opposite of previous reports. The authors argued that the metal electrodes coating the mesa alter the electric field distribution in such a way that the quantum well emission wavelength is altered. Finite-difference time domain (FDTD) calculations were conducted to show how the electric field intensity aligns with the top quantum well at different wavelengths with and without metal contacts. PL measurements of nanowire LEDs with an without metal contacts also shows a clear red-shift in agreement with the EL measurements. While it is not clear how the devices are behaving, it certainly warrants further study.

The device properties of nanoscale LEDs needs to be studied over a much larger length scale, spanning both microscale and nanoscale. Ideally, the devices would be processed and tested in the LIV measurements alone will likely not be sufficient to understand the underlying device physics since there are too many factors coupled together. Not only are internal electric field distributions potentially complicating the emission characteristics, but also strain relaxation, surface losses and surface depletion regions may alter device behavior as the mesa diameters are reduced below the microscale. To better understand device behavior, optical characterization of mesa structures will be conducted in parallel to LIV-based device processing experiments.
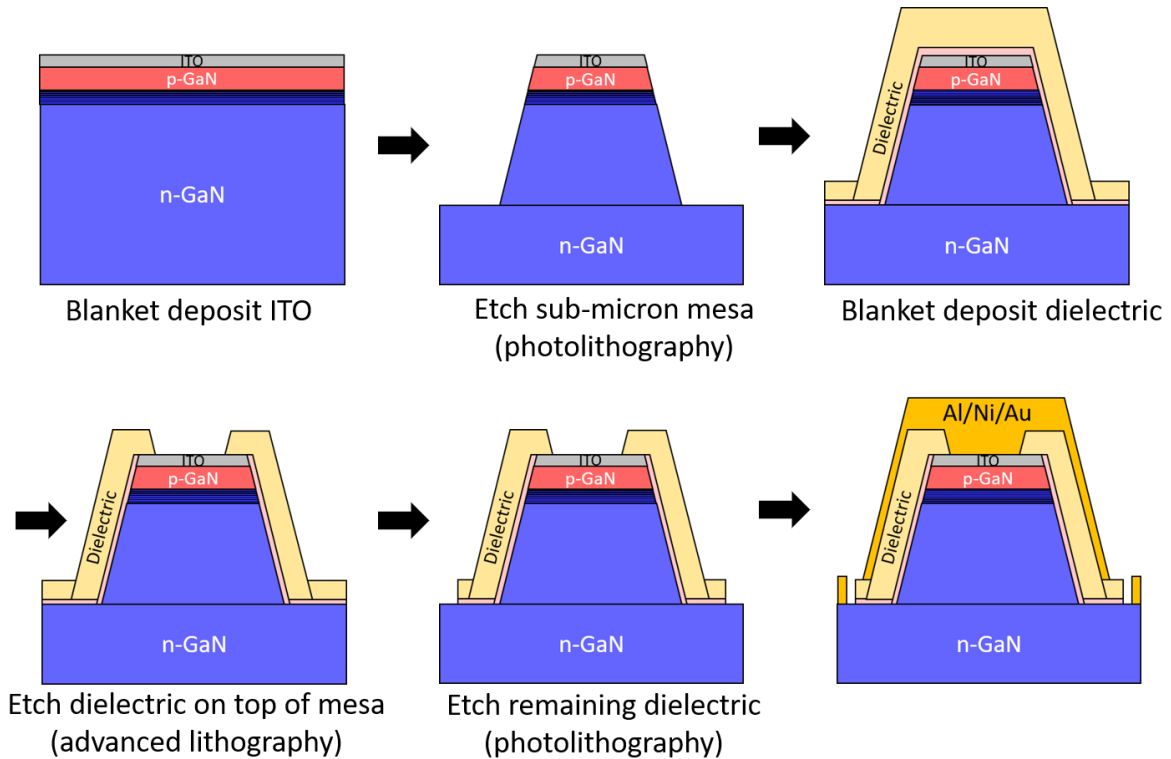
Figure 5.1: Overview of the sub-micron LED nanofabrication process.

5.2   Nanofabrication process

The sub-micron LED process will follow nearly the same microLED fabrication pro-
cess described in chapter 3–only the mesa diameters must span the strain relaxation
regime from Chapter 4 (100 - 1000 nm) in addition to the microscale. The main nanofab-
rication challenges facing nanoscale LEDs are related to the lithography; specifically, the
mesa etch and the dielectric via opening. Not only must the mesas be etched with di-
ameters below 1 μm, but also the dielectric via openings must be aligned within that
region. For example, a 200 nm diameter LED may require a dielectric opening between
50 and 100 nm in diameter with a corresponding alignment tolerance of about 75 and
50 nm. The typical i-line (Hg lamp, $\lambda = 365$ nm) stepper that one finds in university
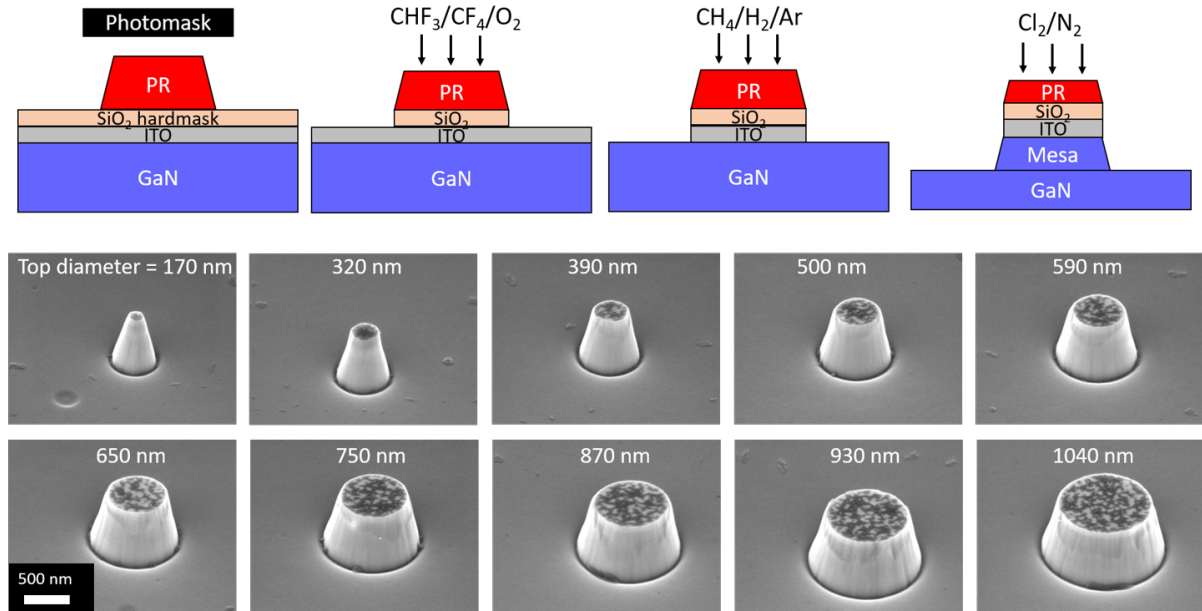
Figure 5.2: Sub-micron mesa etch process schematic with example SEMs of final mesa structures.

cleanrooms struggle to exposure features with dimensions at or below about 500 nm. Even with perfect mechanical positioning and precise optics, diffraction limitations fundamentally become an issue. The exposed light intensity is usually assumed to be zero in regions block off by the photolithography mask, but such a discontinuity of light violates Maxwell's equations since light is a wave. The light intensity actually decays into the dark masked off region, leading to a exposure tail whose length depends on the source wavelength and system geometry. Fortunately for the mesa lithography, this exposure tail is actually advantageous.

To maximize the resolution of the mesa lithography step (without resorting to advanced, non-photolithography schemes), a thin photoresist (SPR955-0.9, $t \sim 900$ nm) on a SiO_2 hardmask was employed. The thin resist allows for more mechanically stable features with larger aspect ratios (diameter relative to height); the SiO_2 prevents over etching the thin resist and offers higher thermal stability to ensure accurate pattern transfer during plasma etching. The mesa etch consisted of a blanket electron beam de-

position of 30 nm of ITO on commercial blue ($\lambda \sim 465$ nm) followed by a blanket sputter deposition of 150 nm SiO_2 as the hardmask. SPR955-0.9 was spin coated and exposed by an i-line stepper ($\lambda = 365$ nm; optimized conditions are: time = 0.53 seconds, focus offset = -0.3).

The next big challenge in realization of sub-micron LEDs is the dielectric via opening, which requires an alignment to the top of the mesa. There are three main options for the lithography, none of which are easy: (1) electron beam lithography, (2) focused ion beam and (3) self-aligned methods. Self-aligned methods have been developed for InGaN microLEDs down to 1 μm in top diameter.[8] This process has the potential to be scaled to smaller dimensions, but perhaps not 100-300 nm diameter and will likely require very lengthy process development.

5.3   Carrier dynamics in sub-micron nanoscale mesas

Sub-micron LED device behavior is expected to become very complicated with additional factors affecting observed LIV trends. For example, the strain relaxation effect should reduce the piezoelectric field in the quantum wells and increase the recombination rates. This effect may also be nonuniform across the mesa, with a higher degree of strain relaxation closest to the outer edge. Sidewall depletion region effects may also introduce variations in the injection efficiency. The mesa dimensions in some cases may be below the wavelength of light emission, leading to more complicated light extraction effects that do not follow ray optics. Due to these considerations, additional characterization of LED properties are needed to decouple if and how these factors may influence LIV behavior. In order to separate carrier dynamics from overall LIV characteristics, optical characterization methods, such as power and temperature dependent photoluminescence (both time-resolved and time-integrated), as well as cathodoluminescence, were all em-

ployed. Photoluminescence tests will give information about the overall carrier dynamics while cathodoluminescence can provide information about the spatial variations in carrier dynamics due to piezoelectric field differences.

Time-integrated PL measurements may be modeled with the steady-state continuity equation:

$$\frac{\partial N}{\partial t} = 0 = G_{laser} - U_{SRH} - U_{rad} - U_{Aug} \tag{5.1}$$

where N is the carrier density, G_{laser} is the carrier generation rate from the laser and the U terms are the three main recombination pathways. Each recombination mechanism may be modeled as:

$$U_{SRH} = \sigma v_{th}(T) N_T \frac{pn - n_i^2}{n + p + 2n_i \cosh \frac{E_t - E_i}{kT}} \tag{5.2}$$

$$U_{rad} = B(np - n_i^2) \tag{5.3}$$

$$U_{Aug} = C(n + p)(np - n_i^2) \tag{5.4}$$

where σ is the carrier capture coefficient, v_{th} is the thermal velocity, N_T is the trap density.

$$\eta_{PL} = \frac{U_{rad}}{U_{SRH} + U_{rad} + U_{Aug}} \tag{5.5}$$

Solving this equation numerically at different temperatures and plotting η_{PL} as a function of carrier density, we can see the expected trend for the PL efficiency.

There have been some limited reports on the diameter-dependent carrier dynamics in nanoscale InGaN mesa structures where Wu *et al.* studied the effect of mesa diameter (d = 120 - 320 nm) on photoluminescence behavior.[38] They employed both time-resolved (TRPL) and time-integrated PL (TIPL) methods at room temperature and at 20 K. The TRPL measurements showed an increase in the overall recombination rate at room temperature and low temperature. The decay rate at 20 K appears linear over the time
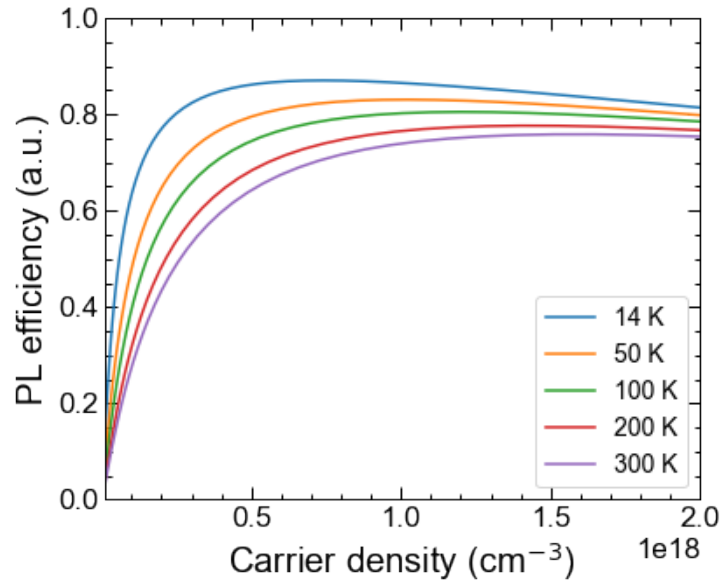
Figure 5.3: Calculated PL efficiency curves at different temperatures for time-integrated PL.

scale reported for the $d = 180$, 220 and 300 nm mesa structures. At 120 nm, however, the TRPL curves seem to decay exponentially over time at 20 K. At room temperature, all the TRPL curves exhibit an exponential-like decay rate as well as showing an overall faster recombination rate in comparison to low temperature measurements.

The TIPL measurements, on the other hand, show opposing trends between low and room temperature conditions. At 20 K, the emission intensity increased with smaller mesa diameters while the room temperature emission intensities decrease below 220 nm. The increased emission intensity at low temperatures could be entirely due to higher laser pump coupling and light extraction efficiency, but the decrease observed at room temperature is likely due to higher nonradiative recombination rates. In the absence of chemical treatments or dielectric passivation schemes to minimize surface-related defect states, it is likely that a large surface recombination rate is dominated the size-dependent dynamics. Now that more advanced passivation schemes are available, this problem may be revisited and studied over a larger suite of mesa diameters.

5.4   Temperature-dependent photoluminescence

At the time of this thesis submission, the time-resolved photoluminescence system was not ready. The time-integrated temperature dependent photoluminescence system, however, was constructed in order to assess the effect of SRH recombination on overall carrier dynamics. The time-integrated temperature dependent PL system (i.e. TDPL) consisted of a 405 nm laser diode pump source which passes through a rotating 405 nm half-wave plate and a polarized beam splitter (PBS). The rotating half-wave plate alters the beam polarization such that the splitting ratio at the PBS may be tuned–effectively tuning the laser beam power that reaches the sample. A small portion of the output beam is deflected onto a photodiode to track the laser power while the majority of the beam is guided to the sample. The sample sits in a cryostat chamber that is liquid helium cooled down to 14 K. The light emission is focused into a fiber optics cable and transported to a spectrometer (Ocean Optics USB4000+). The PL spectra is taken at various laser powers and integrated to yield the PL efficiency as follows:

$$\eta_{PL} \propto \frac{\lambda_p P_{out}}{P_{in}} \tag{5.6}$$

where λ_p is the peak wavelength, P_{out} is the integrated intensity and P_{in} is the laser pump power.

To investigate the influence of surface recombination on overall recombination, samples were characterized before and after etching mesa structures with and without passivation methods discussed in chapter 3. Commercially grown blue and green ($\lambda \sim 465$ and 525 nm, respectively) epi was diced into 1x1 cm2 samples and characterized by TDPL before any processing. Samples were then etched using the Langmuir-Blodgett colloid lithography method with 2530 nm diameter colloids. Samples were then etched in an
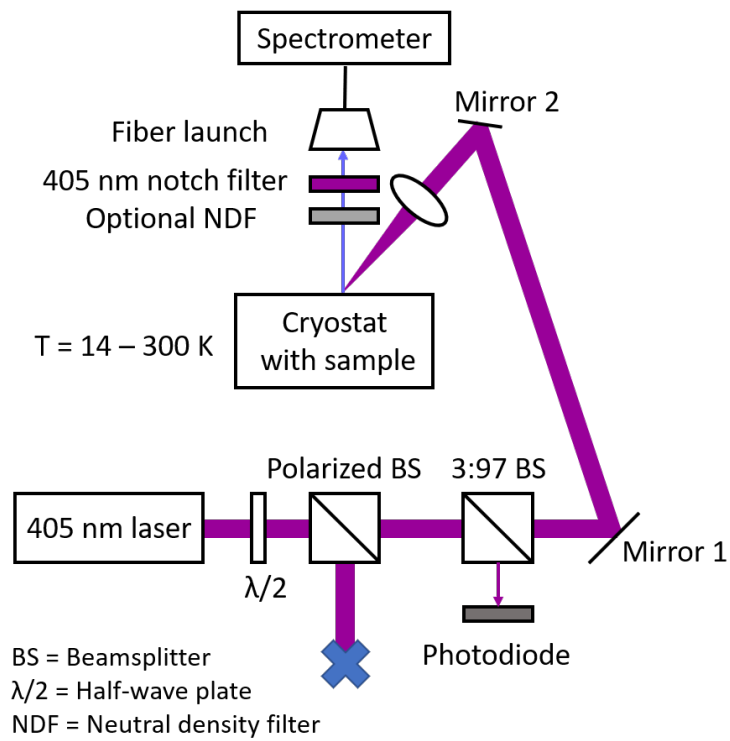
Figure 5.4: Schematic of the temperature dependent photoluminescence system.
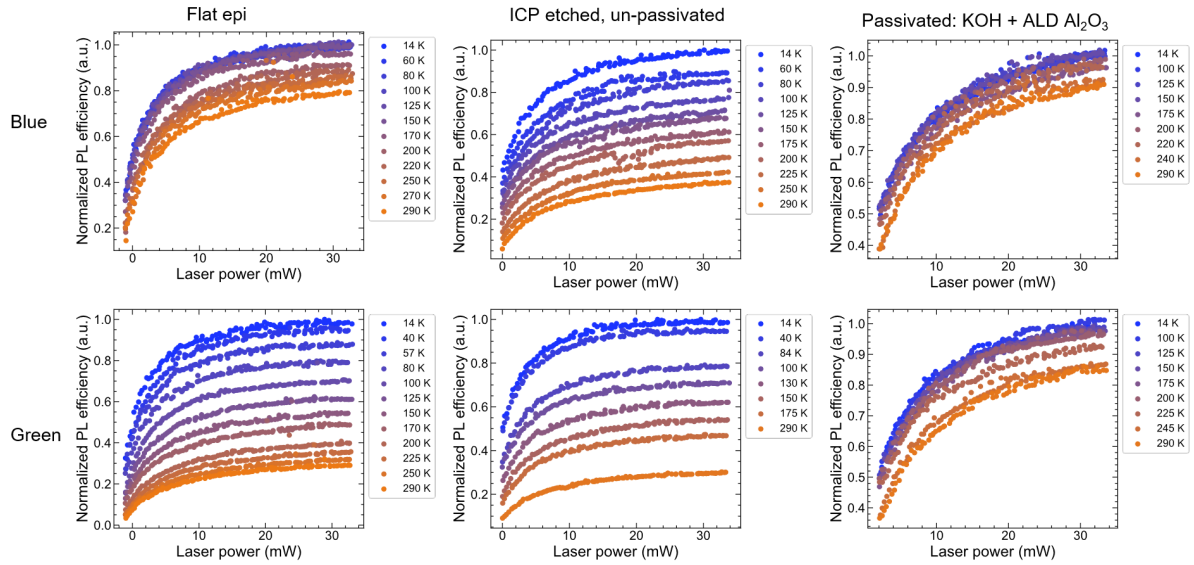
Figure 5.5: Integrated intensities normalized by input power. The top row is for blue epi and the bottom row is from green epi. Each column corresponds to the step of the process where the data was taken.

ICP Cl_2/N_2 plasma to yield a high density of 2.5 μm diameter mesa structures, are not expected to have significant surface recombination losses after chemical treatments and dielectric passivation. TDPL measurements were repeated, and the samples were subjected to room temperature KOH and piranha treatments. They were then passivated by 10 nm ALD Al_2O_3 and characterized by TDPL a third time. Section 5.4 shows all the integrated PL efficiency data calculated by Eq. (5.6).

For the flat blue and green epi, the TDPL characteristics show a decrease in η_{PL} as the temperature is decreased from 290 K to 14 K as expected. Moreover, the decrease in η_{PL} is much more pronounced in the green epi than the blue, which is likely due to the relatively lower crystal quality (i.e. higher defect density) of the green InGaN quantum wells. After ICP etching but before any chemical treatments or passivation, the dispersion in the blue TDPL curves is significantly higher; however, the green sample's TDPL behavior is largely unaffected. This is rather surprising since the surface recombination

58

is expected to be less severe in green InGaN LEDs, and so the TDPL behavior to be less affected by passivation. This warrants further investigation as to why this is occurring. The next steps are to first rule out any influences from the system, such as variations across the sample, condensation at lower temperatures or pump recycling.

5.5   Towards etched quantum-dot InGaN LEDs

An important semiconductor concept is the density of states (DOS), which affects a number of properties, such as light absorption, carrier transport, emission spectra, etc. The DOS describes the number of electron states per unit volume per energy that carriers can occupy. When the dimensionality of a semiconductor material is reduced, the spatial confinement of the electron wavefunctions alters the energy states and thus the DOS. For example, a quantum well in an LED is confined in one direction and is considered a 2D system with discrete energy states in the direction of confinement. In the context of nanoscale LEDs, reducing the mesa diameter may also confine carriers laterally where quantum wells start to resemble quantum dots. The allowed energy levels in the quantum dot-like active region are more discrete, which would be expected to narrow the linewidth of emission. As the mesa diameter is reduced further, the DOS approaches a delta function where only a single energy level is allowed (see Section 5.5 below). As such, the single energy level has the potential to lead to lasing from the LED simply by reducing the mesa diameter.

Quantum dot (QD) based LEDs have been investigated for single-photon sources, LEDs, detectors and laser diodes (LDs).[69, 70] Strained, lattice mismatched materials, such as InGaN/GaN or InAs/GaAs, are also of interest for QD technology due to their ability to potentially relax strain. Chen *et al.*[71] plasma etched QD InGaN/GaN mesas with top diameters around 10 nm and 40 nm, formed via electron beam lithogra-
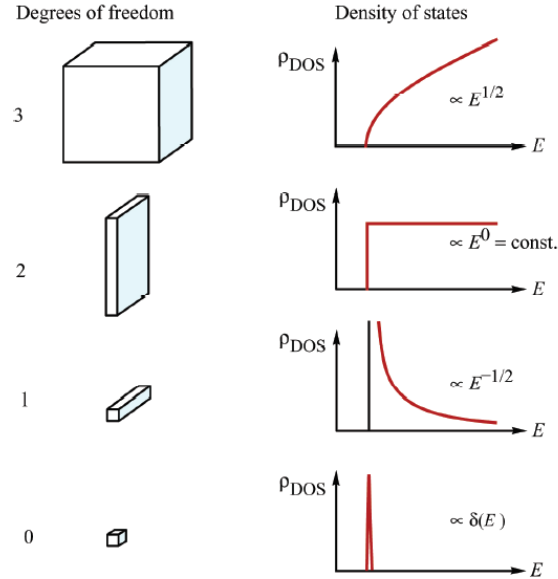
Figure 5.6: Density of states in semiconductors with 3, 2, 1 and 0 degrees of freedom. In a 0D quantum dot system, the DOS approaches a delta function.

phy. PL measurements showed a clear blueshift in the nanoscale mesas with respect to un-patterned epi, which likely is due to a mixture of strain relaxation and quantum confinement. Moreover, the 10 nm mesa exhibited a large blueshift as well as a narrower PL emission linewidth than the 40 nm mesa. The nanoscale mesas relative to un-patterned epi also showed a lower PL photon energy shift versus both excitation power and temperature, suggesting 3D quantum confinement effects are pinning the emission energy. A more recent study by Higo *et al.*[72] also investigated the temperature-dependent carrier lifetimes of QDs versus QWs through TRPL. They found that carrier lifetimes in 5 nm diameter QDs were nearly temperature-independent down to 6 K, suggesting that quantum confinement pins the QD DOS.

These studies are not only limited in number, but they also lack a detailed understanding of the diameter-dependent behavior over a large range of mesa diameters. It is also not clear at what mesa diameter length scales do quantum confinement effects begin to affect emission properties. The mesa etch process developed in this chapter is

well-poised to investigate these effects across a broad range of diameters. Following the dry etch process, solution-based etches may be used not only to remove surface defects, but also to further reduce the mesa diameter to the sub-100 nm regime.

5.6   Conclusion

Sub-micron LED mesas were etched using a conventional, but optimized, photolithography process. A thin photoresist and a dielectric hardmask were used to maximize the lithography resolution while providing thermal and mechanical stability during plasma etching. The dielectric via etch, at the time of this thesis, is being actively investigated. The two most promising options are electron-beam lithography and focused ion beam etching, which are suitable for breaking through limitations of university-level photolithography resolutions. Next, the effect of mesa size reduction on carrier dynamics was being investigated through photoluminescence techniques. A temperature and power-dependent PL system was constructed and automated. Preliminary measurements were conducted with some unexpected results that warrant further investigation.

Chapter 6

Conclusion

MicroLEDs are well-poised to replace state-of-the-art LCD and OLED-based displays. However, there are several challenges that need to be overcome before microLED displays may be commercialized. There are significant efficiency losses that arise when the mesa dimensions are reduced to the necessary pixel sizes (1 - 5 μm), and producing an efficient red microLED is especially difficult. AlGaInP-based red light emitters suffer from far more serious surface recombination losses than the III-nitride material family, but red InGaN-based LEDs are notoriously difficult to grow due to the 11 % lattice mismatch between InN and GaN. Not only does this lead to reduced crystal quality, but the lattice mismatch also gives rise to large piezoelectric fields that lower the radiative efficiency and cause unstable emission wavelengths. Nanopatterning InGaN/GaN material is a potential route for mitigating some of the consequences, but is not a viable solution if the surface recombination losses are significant.

Surface recombination losses in blue InGaN microLEDs were minimized using dielectric passivation and solution-based KOH etching. A cleanroom process was developed to fabricate flip-chip-based microLEDs with mesa diameters spanning 2-100 μm. To quantify the EQE behavior, a high sensitivity optoelectronic device testing system was

constructed that may perform on-chip measurements without packaging each LED onto a silver header. The system utilized a thermoelectrically cooled detector that may measure incredibly small amounts of light (~ 10 pW lower limit). Upon minimization of the surface recombination losses, enhanced light extraction efficiency was revealed to increase the EQE in smaller devices.

Chemical etching and Al_2O_3 dielectric passivation were used to minimize non-radiative sidewall defects in InGaN/GaN microLEDs (mesa diameter = 2-100 μm), resulting in an increase in external quantum efficiency (EQE) as LED size was decreased. Peak EQEs increased from 8-10% to 12-13.5% for mesa diameters from 100 μm to 2 μm, respectively, and no measurable leakage currents were seen in current density-voltage (J-V) characteristics. The position and shape of EQE curves for all devices were essentially identical, indicating size-independent ABC model (Shockley-Read-Hall, radiative, and Auger recombination) coefficients–behavior that is not typical of microLEDs as size decreases. These trends can be explained by enhancement in light extraction efficiency (LEE), which is only observable when sidewall defects are minimized, for the smallest LED sizes. Detailed ray-tracing simulations substantiate the LEE enhancements.

Next, strain in InGaN/GaN multiple-quantum well (MQW) light emitters was relaxed via nanopatterning using colloidal lithography and top-down plasma etching. Colloidal lithgraphy was performed using Langmuir-Blodgett dip-coating of samples with silica particles (d = 170, 310, 690, 960 nm) and a Cl_2/N_2 inductively coupled plasma etch to produce nanorod structures. The InGaN/GaN MQW nanorods were characterized using x-ray diffraction (XRD) reciprocal space mapping (RSM) to quantify the degree of relaxation. A peak relaxation of 32 % was achieved for the smallest diameter features tested (120 nm after etching). Power-dependent photoluminescence at 13 K showed blue-shifted quantum well emission upon relaxation, which is attributed to reduction of the inherent piezoelectric field in the III-nitrides. Poisson-Schrödinger simulations of

single well structures also predicted increasing spectral blueshift with strain relaxation, in agreement with experiments.

Finally, the microLED device process from chapter 3 was extended to the nanoscale regime where strain relaxation may occur. An etch process was developed that can produce mesa structures with diameters down to about 200 nm using by optimizing the resolution of a photolithography process. Electron-beam lithography and focused ion beam etching techniques were being investigated as potential routes for etching dielectric via openings to finish the process. In parallel to the device processing, a temperature and power dependent photoluminescence system was constructed to better understand the influence of sub-micron patterning on the carrier dynamics.

As for continuing the research presented in this thesis, both the device processing and optical characterization are incredibly important. The process is nearly complete; we just need to poke a hole in the dielectric on top of the mesa. With the help of the cleanroom staff who specialize in advanced lithography techniques, I believe this is very achievable with a potential to open the door for a bounty of scientific riches. On the characterization side, continuation of the temperature-dependent PL on both microscale and nanoscale mesa structures is the next step. Complementing these studies with time-resolved PL and cathodoluminescence will also greatly help understand the carrier dynamics. Additionally, finite-difference time domain (FDTD) modeling of nanoscale LEDs has the potential to unveil some interesting extraction properties that may affect emission wavelength characteristics.[68]

Bibliography

1. Nakamura, S., Harada, Y. & Seno, M. Novel metalorganic chemical vapor deposition system for GaN growth. *Appl. Phys. Lett.* **58** (1991).

2. Nakamura, S. GaN growth using GaN buffer layer. *Jpn. J. Appl. Phys.* **30,** L1705 (1991).

3. Nakamura, S., Mukai, T. & Senoh, M. Thermal annealing effects on p-type Mg-doped GaN films. *Jpn. J. Appl. Phys.* **31,** L139–L142 (1992).

4. Nakamura, S., Iwasa, N., Senoh, M. & Mukai, T. Hole compensation mechanism of p-type GaN films. *Jpn. J. Appl. Phys.* **31,** 1258–1266 (1992).

5. Nakamura, S. & Mukai, T. High-quality InGaN films grown on GaN films. *Jpn. J. Appl. Phys.* **31,** L1457 (1992).

6. Nakamura, S., Mukai, T. & Senoh, M. Candela-class high-brightness InGaN/AlGaN double-heterostructure blue-light-emitting diodes. *Jpn. J. Appl. Phys.* **64,** 1687 (1994).

7. National Research Council. *Assessment of Advanced Solid-State Lighting* (The National Academies Press, Washington, DC, 2013).

8. Smith, J. M. *et al.* Comparison of size-dependent characteristics of blue and green InGaN microLEDs down to 1 μm in diameter. *Appl. Phys. Lett.* **116,** 071102 (2020).

9. Schubert, E. F. *Light-Emitting Diodes* chap. 2 (Cambridge Press, 2003).

10. Ley, R. T. *et al.* Revealing the importance of light extraction efficiency in In-GaN/GaN microLEDs via chemical treatment and dielectric passivation. *Appl. Phys. Lett.* **116,** 251104 (2020).

11. Dingle, R., Sell, D. D., Stokowski, S. E. & Ilegems, M. Absorption, reflectance, and luminescence of GaN epitaxial layers. *Phys. Rev. B Condens. Matter* **4,** 1211–1218 (1971).

12. Nakamura, S. The Roles of Structural Imperfections in InGaN-Based Blue Light–Emitting Diodes and Laser Diodes. *Science* **281,** 956–961 (1998).

13. Ding, K., Avrutin, V., Izyumskaya, N., Ozgur, U. & Morkoc, H. MicroLEDs, a Manufacturability Perspective. *Applied Sciences* **9,** 1206 (2019).

14. Paranjpe, A., Montgomery, J., Lee, S. M. & Morath, C. Micro-LED Displays: Key Manufacturing Challenges and Solutions. *SID Symposium Digest of Technical Papers* **49,** 597–600 (2018).

15. Tian, P. *et al.* Size-dependent efficiency and efficiency droop of blue InGaN micro-light emitting diodes. *Appl. Phys. Lett.* **101,** 231110 (2012).

16. Olivier, F. *et al.* Influence of size-reduction on the performances of GaN-based microLEDs for display application. *J. Lumin* **191,** 112–116 (2017).

17. Olivier, F., Daami, A., Licitra, C. & Templier, F. Shockley-Read-Hall and Auger non-radiative recombination in GaN based LEDs: A size effect study. *Appl. Phys. Lett.* **111,** 022104 (2017).

18. Hwang, D., Mughal, A., Pynn, C. D., Nakamura, S. & DenBaars, S. P. Sustained high external quantum efficiency in ultrasmall blue III–nitride micro-LEDs. *Appl. Phys. Express* **10,** 032101 (2017).

19. C. G. Van de Walle and D. Segev. Microscopic origins of surface states on nitride surfaces. *J. Appl. Phys* **101,** 81704 (2007).

20. Shul, R. J. *et al.* Inductively coupled plasma-induced etch damage of GaN p-n junctions. *J. Vac. Sci. Technol. A* **18,** 1139–1143 (2000).

21. .

22. Hartensveld, M., Ouin, G., Liu, C. & Zhang, J. Effect of KOH passivation for top-down fabricated InGaN nanowire light emitting diodes. *J. Appl. Phys.* **126,** 183102 (2019).

23. Wong, M. S. *et al.* High efficiency of III-nitride micro-light-emitting diodes by side-wall passivation using atomic layer deposition. *Optics Express* **26,** 21324–21331 (2018).

24. Wong, M. S. *et al.* Size-independent peak efficiency of III-nitride micro-light-emitting-diodes using chemical treatment and sidewall passivation. *Appl. Phys. Express* **12,** 097004 (2019).

25. Choi, H. W. *et al.* Mechanism of enhanced light output efficiency in InGaN-based microlight emitting diodes. *J. Appl. Phys.* **93,** 5978–5982 (2003).

26. Bulashevich, K. A., Konoplev, S. S. & Karpov, S. Y. Effect of die shape and size on performance of III-nitride microLEDs: a modeling study. *Photonics* **5,** 41 (2018).

27. Ping, A. T., Chen, Q., Yang, J. W., Khan, M. A. & Adesida, I. The effects of reactive ion etching-induced damage on the characteristics of ohmic contacts to n-type GaN. *J. Electron. Mater.* **27,** 261–265 (1998).

28. Lee, S. W. *et al.* Origin of forward leakage current in GaN-based light emitting devices. *Appl. Phys. Lett.* **89,** 132117 (2006).

29. Kuksenkov, D. V., Temkin, H., Osinsky, A., Gaska, R. & Khan, M. A. Origin of conductivity and low-frequency noise in reverse-biased GaN *p-n* junction. *Appl. Phys. Lett.* **72,** 1365 (1998).

30. Sze, S. *Physics of Semiconductor Devices* chap. 2 (John Wiley & Sons, 2007).

31. Gong, Z. *et al.* Size-dependent light output, spectral shift, and self-heating of 400 nm InGaN light- emitting diodes. *J. Appl. Phys.* **107** (2010).

32. Zhuang, D. & Edgar, J. H. Wet etching of GaN, AlN, and SiC: a review. *Mater. Sci. Eng. R Rep.* **48,** 1–46 (2005).

33. Tautz, M. & Diaz, D. D. Wet-chemical etching of GaN: underlying mechanism of a key step in blue and white LED production. *ChemistrySelect* **3,** 1480–1494 (2018).

34. Henry, W. & Percival, C. ILED displays: next generation display technology. *SID Symposium Digest of Technical Papers* **47,** 747–750 (2016).

35. Baumeister, P. W. Optical tunneling and its application to optical filters. *Appl. Opt.* **6,** 897–905 (1967).

36. Krames, M. R. *et al.* Status and future of high-power light emitting diodes for solid-state lighting. *J. Disp. Technol.* **3,** 160–175 (2007).

37. Ley, R. *et al.* Strain relaxation of InGaN/GaN multi-quantum well light emitters via nanopatterning. *Opt. Express* **27,** 30081–30089 (2019).

38. Wu, Y.-R., Chiu, C., Chang, C.-Y., Yu, P. & Kuo, H.-C. Size-dependent strain relaxation and optical characteristics of InGaN/GaN nanorods LEDs. *J. Sel. Top. Quantum Electron* **15,** 1226–1233 (2009).

39. Ee, Y.-K. *et al.* Optimzation of light extraction efficiency of III-nitride LEDs with self-assembled colloidal-based microlenses. *IEEE J. Sel. Top. Quantum Electron.* **15,** 1218–1225 ().

40. Hsieh, M.-Y. *et al.* Improvement of external extraction efficiency in GaN-based LEDs by SiO$_2$ nanosphere lithography. *IEEE Electron Device Lett.* **29,** 658–660 (2008).

41. Hsieh, M.-Y., Wang, C.-Y., Chen, L.-Y., Ke, M.-Y. & Huang, J. J. InGaN-GaN nanorod light emitting arrays fabricated by silica nanomasks. *IEEE J. Quantum Electron.* **44,** 468–472 (2008).

42. Ng, W. N., Leung, C. H., Lai, P. T. & Choi, H. W. Nanostructuring GaN using microsphere lithography. *J. Vac. Sci. Technol. B* **26,** 76–79 (2008).

43. Fu, W. Y., Wong, K. K.-Y. & Choi, H. W. Close-packed hemiellipsoid arrays: A photonic band gap structure patterned by nanosphere lithography. *Appl. Phys. Lett.* **95,** 133125 (2009).

44. Pynn, C. D. *et al.* Enhanced light extraction from free-standing InGaN/GaN. *Opt. Express* **25,** 15778 (2017).

45. Wang, C.-Y. *et al.* GaN nanorod light emitting diode arrays with a nearly constant electroluminescent peak wavelength. *Optics Express* **16** (2008).

46. Li, Q. *et al.* Optical performance of top-down fabricated InGaN/GaN nanorod light emitting diode arrays. *Opt. Express* **19,** 25528 (2011).

47. Latzel, M. *et al.* Significant performance enhancement InGaN/GaN nanorod LEDs with multi-layer graphene transparent electrodes by alumina surface passivation. *Nanotechnology* **28,** 055201 (2017).

48. Chen, L.-Y. *et al.* High performance InGaN/GaN nanorod light emitting diode arrays fabricated by nanosphere lithography and chemical mechanical polishing processes. *Optics Express* **18,** 7664–7669 (2010).

49. Truong, T. A. *et al.* Light extraction from GaN-based light emitting diode structures with a noninvasive two-dimensional photonic crystal. *Appl. Phys. Lett.* **94,** 023101 (2009).

50. Keller, S. *et al.* Optical and structural properties of GaN nanopillar and nanostripe arrays with embedded multi-quantum wells. *J. Appl. Phys.,* 054314 (2006).

51. Keller, S. *et al.* Optical properties of GaN nanopillar and nanostripe arrays with embedded InGaN/GaN multi quantum wells. *Phys. status solidi,* 1797–1801 (2007).

52. Tend, C. H., Zhang, L., Deng, H. & Ku, P. C. Strain-induced red-green-blue wavelength tuning in InGaN quantum wells. *Appl. Phys. Lett.* **108,** 071104 (2016).

53. Reddy, N. P. *et al.* Enhanced luminescence from GaN nanopillar arrays fabricated using a top-down process. *Nanotechnology* **27,** 065304 (2016).

54. Ramesh, V., Kikuchi, A., Kishino, K., Funato, M. & Kawakami, Y. Strain relaxation effect by nanotexturing InGaN/GaN multiple quantum well. *J. Appl. Phys.* **107,** 114303 (2010).

55. Wang, Q. *et al.* Diameter-dependent photoluminescence properties of strong phase-separated dual-wavelength InGaN/GaN nanopillar LEDs. *Appl. Surf. Sci.* **410,** 196–200 (2017).

56. Pereira, S *et al.* Strain and composition distributions in wurtzite InGaN/GaN layers extracted from x-ray reciprocal space mapping. *Appl. Phys. Lett.* **80,** 3913 (2002).

57. Zhuang, Z. *et al.* Great enhancement in the excitonic recombination and light extraction of highly ordered InGaN/GaN elliptic nanorod arrays on a wafer scale. *Nanotechnology* **27,** 015301 (2016).

58. Wang, Q, Bai, J, Wang, Y. P. G. & Wang, T. Influence of strain relaxation on the optical properties of InGaN/GaN multiple quantum well nanorods. *J. Phys. D. Appl. Phys.,* 395102 (2011).

59. Miller, D. *et al.* Band-edge electroabsorption in quantum well structures: the quantum-confined Stark effect. *Phys. Rev. Lett.* **53,** 2173–2176 (1984).

60. Gonzalez, F. L., Chan, L., Berry, A., Morse, D. E. & Gordon, M. J. Simple colloidal lithography method to fabricate large-area moth-eye antireflective structures on Si, Ge and GaAs for IR applications. *J. Vac. Sci. Technol. B* **32,** 051213 (2014).

61. Young, E. C., Romanov, A. E. & Speck, J. S. Determination of composition and lattice relaxation in semipolar ternary (In,Al,Ga)N strained layers from symmetric x-ray diffraction measurements. *Appl. Phys. Express* **4,** 061001 (2011).

62. Wright, A. F. Elastic properties of zinc-blende and wurtzite AlN, GaN and InN. *J. Appl. Phys.* **82,** 2833–2839 (1997).

63. Roesener, T., Klinger, V., Weuffen, C., Lackner, D. & Dimroth, F. Determination of heteroepitaxial layer relaxation at growth temperature from room temperature x-ray reciprocal space maps. *J. Cryst. Growth* **368,** 21–28 (2013).

64. Moram, M. A. & Vickers, M. E. X-ray diffraction of III-Nitrides. *Rep. Prog. Phys.* **72,** 036502 (2009).

65. Hahn, Y. *et al.* High-density plasma-induced etch damage of InGaN/GaN multiple quantum well light- emitting diodes. *J. Appl. Phys.* **921,** 1189–1139 (2002).

66. Bulashevich, K. A. & Karpov, S. Y. Impact of Surface Recombination on Efficiency of III-Nitride Light Emitting Diodes. *Phys. Status Solidi RRL* **10,** 480–484 (2016).

67. Sala, F. D. *et al.* Free-carrier screening of polarization fields in wurtzite GaN/InGaN laser structures. *Appl. Phys. Lett.* **74** (1999).

68. Zhang, G. *et al.* Single nanowire green InGaN/GaN light emitting diodes. *Nanotechnology* **27,** 435205 (2016).

69. Arakawa, Y. & Holmes, M. J. Progress in quantum-dot single photon sources for quantum information technologies: a broad spectrum overview. *Appl. Phys. Rev.* **7,** 021309 (2020).

70. Norman, J. C. *et al.* A review of high-performance quantum dot lasers on silicon. *IEEE J. Quantum Electron.* **55** (2019).

71. Chen, H.-S. *et al.* Strain relaxation and quantum confinement in InGaN/GaN nanoposts. *Nanotechnology* **17,** 1454 (2005).

72. Higo, A. *et al.* Optical study of sub-10 nm $In_{0.3}Ga_{0.7}N$ quantum nanodisks in GaN nanopillars. *ACS Photonics* **4,** 1851–1857 (2018).